JAERI-M
88-102

INDC (JPN) 115/G
NEANDC (J) 129/A

MEASUREMENT OF DOUBLE DIFFERENTIAL NEUTRON EMISSION CROSS SECTIONS AT 14.1 MeV FOR ^{209}Bi, ^{10}B AND ^{11}B

June 1988

Akito TAKAHASHI*, Yasuhiro SASAKI* and Hisashi SUGIMOTO*

日 本 原 子 力 研 究 所
Japan Atomic Energy Research Institute

JAERI-M レポートは，日本原子力研究所が不定期に公刊している研究報告書です。
入手の問合わせは，日本原子力研究所技術情報部情報資料課（〒319-11茨城県那珂郡東海村）あて，お申しこしください。なお，このほかに財団法人原子力弘済会資料センター（〒319-11 茨城県那珂郡東海村日本原子力研究所内）で複写による実費頒布をおこなっております。

JAERI-M reports are issued irregularly.
Inquiries about availability of the reports should be addressed to Information Division Department of Technical Information, Japan Atomic Energy Research Institute, Tokai-mura, Naka-gun, Ibaraki-ken 319-11, Japan.

編集兼発行　日本原子力研究所
印　　刷　いばらき印刷㈱

Measurement of Double Differential Neutron Emission Cross Sections at 14.1 MeV for ^{209}Bi, ^{10}B and ^{11}B

Akito TAKAHASHI*, Yasuhiro SASAKI* and Hisashi SUGIMOTO*

Department of Physics
Tokai Research Establishment
Japan Atomic Energy Research Institute
Tokai-mura, Naka-gun, Ibaraki-ken

(Received May 12, 1988)

Double differential neutron emission cross sections at En = 14.1 MeV have been measured for ^{209}Bi, ^{10}B and ^{11}B, using an 8.3 m neutron TOF facility of OKTAVIAN at Osaka University. Data have been taken for 16 angle-points from 15° to 160° in the laboratory angle, with the covering energy region of secondary neutrons from 0.5 MeV to 14 MeV. The overall energy resolution of experiment was ± 0.2 MeV. By integrating measured double differential data over either laboratory or center-of-mass system angles, angle-integrated neutron emission spectra were deduced. Angle-differential cross sections of resolved discrete excited states (elastic, some of discrete inelastic scattering) and Bi(n,2n) reaction were also deduced. Numerical data tables and graphs of these data are given in this report.

In graphs, comparisons are made with evaluated nuclear data, i.e., ENDL-86 for ^{209}Bi and JENDL-3T for ^{10}B and ^{11}B. Discrepancy with the experiment is obvious for the ^{209}Bi evaluation of ENDL-86. The JENDL-3T evaluations for boron isotopes are successful as a whole, however, disagreements with the experiments are seen in the lower secondary energy regions than ca. 5 MeV for emission spectra and in differential elastic scattering cross sections for ^{11}B.

This report is written by summarizing the effort implemented under the Research-in-Trust in 1987 fiscal year from the Japan Atomic Energy Research Institute.

* Osaka University

Keywords: Double Differential Neutron Emission Cross Sections, 14.1 MeV, ^{209}Bi, ^{10}B, ^{11}B, Angle-integrated Spectra, Angle-Differential Cross Sections, ENDL-86, JENDL-3T

^{209}Bi，^{10}B，^{11}Bの14.1 MeVにおける中性子放出二重微分断面積の測定

日本原子力研究所東海研究所物理部
高橋　亮人*・佐々木泰裕*・杉本　久司*

（1988年5月12日受理）

大阪大学オクタビアン付設の8.3 m中性子飛行時間分析装置を置いて，14.1 MeVにおける^{209}Bi，^{10}B，^{11}Bの中性子放出二重微分断面積が測定された。データは，実験室系角度で15度から160度にわたり16点について得られ，測定二次中性子エネルギー範囲は0.5 MeVから14 MeVである。測定系全体のエネルギー分解能は±0.2 MeVであった。測定された二重微分断面積を角度積分して，実験室系及び重心系の角度積分した中性子放出スペクトルが求められた。弾性散乱及び分離された離散非弾性散乱については，角度微分断面積が求められた。又Bi（n，2n）の微分断面積も求められた。グラフ表示も与えられている。

グラフにおいては，ENDL－86のBiの評価データ及びJENDL－3Tの^{10}Bと^{11}Bの評価データと比較している。Biについては，実験値はENDL－86との不一致が目立った。BについてのJENDL－3Tのデータは，概略的には実験と一致しているようであるが，5 MeV以下の低エネルギーでの不一致がある。

本報告書は，日本原子力研究所からの昭和62年度委託研究で行われた成果をまとめたものである。
東海研究所：〒319－11 茨城県那珂郡東海村白方字白根2－4
＊大阪大学

Contents

目　　次

1. INTRODUCTION

Accurate data of double differential neutron emission cross sections for the incident neutron energy of 10 to 15 MeV have been requested[1] for many candidate elements of D-T fusion reactors. It has been regarded that these double differential data are quite useful to assess newly evaluated nuclear data, i. e., JENDL-3, ENDF/B-VI and EFF-2, for application to the fusion reactor technology.

Bismuth is candidated as a neutron multiplier of tritium-breeding blankets. Therefore, differential neutron emission data are of importance as well as ^{209}Bi(n,2n) cross section values. Boron is expected as shielding material of fusion reactors, and its ceramics (boron-nitride) may be used as insulator. Therfore, differential neutron emission data for boron isotopes are of importance from view-points of shielding and radiation damage. Experimental data of differential neutron emission for these three elements are scarcely available or not accurate enough.

To provide accurate and precise experimental data of double differential neutron emission cross sections at incident neutron energy of 14.1 MeV for many candidate elements, a series of measurements is under way[2,3] at the OKTAVIAN facility of Osaka University. Under the financial support of the Japan Atomic Energy Research Institute, measurements for ^{209}Bi, ^{10}B and ^{11}B have been carried out at Osaka University and are reported in this paper. Measured double differential data are tabulated with the EXFOR format. Data are given at 16 angle-points for each element. By integrating double differential data over scattering angles in either laboratory system or center-of-mass system, angle-intergated neutron emission spectra have been deduced and also tabulated with the EXFOR format. The angle-integrated emission spectrum in the center-of-mass system is particularly useful to assess evaluated nuclear data for partial cross section values of specified excited states. Some of elastic and discrete inelastic scattering could be resolved in double differential data, so that angle-differential cross sections were deduced and are given as numerical data tables. Utilization of these data for assessment of evaluated data or nuclear model calculations is beyond the present report. However, preliminary comparisons are made with ENDL-86[4] for Bi, and JENDL-3T*[5] for boron isotopes, and shown in graphs.

* JENDL-3T is a temporary file for testing the evaluated data which are for JENDL-3. The data in JENDL-3T will be partly revised in JENDL-3.

2. EXPERIMENTAL

2.1 Time-of-flight spectrometer

Experimental method is described in detail elsewhere[2]. Only a brief explanation is given in this report. A schematic view of TOF spectrometer is shown in Fig.I-1. The OKTAVIAN accelerator was operated with pulsed deuteron beam of 2 ns pulse width and 1 MHz repetition, and 14 MeV neutrons were generated at the TiT target (T-Target in Fig.I-1). An 8.3 m long TOF facility was constructed in the 85° direction against the deuteron beam line, so as nearly to fix incident neutron energy at 14.1 MeV. A cylindrical scattering sample is set up on an arch (see the insert of Fig.I-1) which locates at 17 cm radially apart from the T-Target center. The cylinder is set up perpendicularly to the arch line, and moved along the arch to change scattering angle. Scattered neutrons by the cylindrical sample are detected with an NE213 liquid scintillator of 25.4 cm diameter and 10 cm thickness. Separability of γ-ray background by the pulse shape discrimination technique is excellent for this detector[2], for a relatively wide dynamic range of 0.5 MeV to 14 MeV in recoil proton energy. A specially shaped shadow bar and a collimator-shield system can serve for sufficiently eliminating backgrounds of direct source neutrons and room-scattered neutrons which are both time-dependent. Background run is done by removing the cylindrical sample. The circuit diagram of measuring system is rather conventinal and shown elsewhere[2].

Incident neutron energy varies very slightly, from 14.2 MeV at 0° to 14.02 MeV at 180°, according to the change of scattering angle. The variation of incident neutron energy was precisely measured by observing elastic scattering peaks at various scattering angles for many samples. The result is shown in Fig.I-2. Since the variation is well within one standard deviation of energy resolution, one can say that the incident neutron energy is fixed to be 14.1 MeV.

Double differential data were measured for 16 angle-points, i. e., 15°, 20°, 30°, 40°, 50°, 60°, 70°, 80°, 90°, 100°, 110°, 120°, 130°, 140°, 150° and 160° in the laboratory system. To obtain absolute cross section values, calibration runs with a 1.5 cm diameter 5 cm long polyethylene cylinder were done[2].

2.2 Samples

For bismuth, natural metal which is 100 % ^{209}Bi was used. The size of

cylinder is 3 cm in diameter and 7 cm in length.

For ^{10}B, powder of 90.4 % enriched ^{10}B metal was canned in a 0.1 mm thick aluminum pipe case which dimensions are 3 cm in diameter and 7 cm in length. This sample contains 9.6 % impurity of ^{11}B, so that correction (subtraction) was made for measured double differential data by using those of ^{11}B sample. However, this correction was small, compared with statisics.

For ^{11}B, metal flake of 98.5 % enriched ^{11}B was canned in a 0.1 mm thick aluminum pipe case with 3 cm in diameter and 7 cm in length. Correction for 1.5 % impurity was ignored in this case. Background run with empty aluminum case was done. However, no visible effect was observed compared with the case removing any sample.

2.3 Multiple scattering correction

Multiple scattering correction was carried out with the MUSCC3 code[6] which is based on a multi-point collision probability method. DDX-type data sets are required for this calculation. DDX-type data sets were generated from evaluated nuclear data files, using the processing code DDXS[7], for a 135 group structure. For bismuth, the evaluated data in ENDL-86[4] was used. For ^{10}B and ^{11}B, the evaluated data in JENDL-3T were used. Multiple scattering correction for the polyethylene sample is incorporated in the MUSCC3 code to result in getting final correction factors. Calculated correction factors were around unity within ca. 10 % deviations for most energy groups, except the energy regions where double differential neutron emission spectra drew steep valleys.

Since the energy distribution of incident neutrons from the TiT target assembly has a parasitic low energy tail as shown in Fig.I-3, correction for measured double differential data is needed to take out this parasitic component. This correction can be done by comparing calculations of multiple scattering flux components between a pure monochromatic and a contaminated source condition. This is also done in the MUSCC3 code. The effect of this parasitic low energy neutrons is significant in low energy region of secondary neutrons, especially for light elements (boron, for example), and not negligible for heavy elements like Bi.

2.4 Other data processing

Angle-integrated neutron emission spectrum in the laboratory system (EDX-in-LAB) is obtained by directly integrating double differential data

for 16 measured angle-points. This was done.

To obtain angle-integrated neutron emission spectrum in the center-of-mass system (EDX-in-CMS), conversion of DDX (double differential cross section) from the LAB system to the CMS was carried out, by supposing the kinematics of inelastic scattering for pseudo-excitation levels which were defined by discretizing the secondary energy region of 0.0 to 14.1 MeV with 0.2 MeV interval. The secondary neutron energy $E_{n'cms}$ in the CMS is written by

$$E_{n'cms} = E_n /(1 + 1/A)^2 - Q_i /(1 + 1/A) \qquad (1)$$

where E_n is the incident neutron energy (14.1 MeV), Q_i the pseudo-excitation energy and A the relative mass of target nucleus, respectively. After this conversion, DDX in the CMS was integrated over coreesponding scattering angles in the CMS to obtain EDX-in-CMS.

Angle-differential cross sections for resolved discrete excited states in measured DDX data were deduced by calculating peak area within an energy bin which was specified with the energy resolution of experiment.

3. RESULTS AND DISCUSSIONS

Numerical data tables of angle-differential cross sections for resolved reaction channels are given in Table 1 through Table 3.

Graphs of DDX data are given in Fig.DF-1 through Fig.DF-15 for ^{209}Bi, Fig.DF-16 through Fig.DF-31 for ^{10}B, and Fig.DF-32 through Fig.DF-47 for ^{11}B. Graphs of angle-integrated neutron emission spectra are given in Fig.EF-1 through Fig.EF-6. Graphs of angle-differential cross sections are given in Fig.AF-1 through Fig.AF-9.

In graphs, evaluated neutron data (ENDL-86 for Bi, JENDL-3T for boron) are also drawn with solid histograms which were used for the multiple scattering corrections with the MUSCC3 code.

To find trends of experimental data in comparison with evaluated data, we can first see angle-integrated neutron emission data in the center-of-mass system, then look through details in correlation with angular dependences of DDX data or angle-differential data.

for 16 measured angle-points. This was done.

To obtain angle-integrated neutron emission spectrum in the center-of-mass system (EDX-in-CMS), conversion of DDX (double differential cross section) from the LAB system to the CMS was carried out, by supposing the kinematics of inelastic scattering for pseudo-excitation levels which were defined by discretizing the secondary energy region of 0.0 to 14.1 MeV with 0.2 MeV interval. The secondary neutron energy $E_{n'cms}$ in the CMS is written by

$$E_{n'cms} = E_n /(1 + 1/A)^2 - Q_i /(1 + 1/A) \qquad (1)$$

where E_n is the incident neutron energy (14.1 MeV), Q_i the pseudo-excitation energy and A the relative mass of target nucleus, respectively. After this conversion, DDX in the CMS was integrated over coreesponding scattering angles in the CMS to obtain EDX-in-CMS.

Angle-differential cross sections for resolved discrete excited states in measured DDX data were deduced by calculating peak area within an energy bin which was specified with the energy resolution of experiment.

3. RESULTS AND DISCUSSIONS

Numerical data tables of angle-differential cross sections for resolved reaction channels are given in Table 1 through Table 3.

Graphs of DDX data are given in Fig.DF-1 through Fig.DF-15 for ^{209}Bi, Fig.DF-16 through Fig.DF-31 for ^{10}B, and Fig.DF-32 through Fig.DF-47 for ^{11}B. Graphs of angle-integrated neutron emission spectra are given in Fig.EF-1 through Fig.EF-6. Graphs of angle-differential cross sections are given in Fig.AF-1 through Fig.AF-9.

In graphs, evaluated neutron data (ENDL-86 for Bi, JENDL-3T for boron) are also drawn with solid histograms which were used for the multiple scattering corrections with the MUSCC3 code.

To find trends of experimental data in comparison with evaluated data, we can first see angle-integrated neutron emission data in the center-of-mass system, then look through details in correlation with angular dependences of DDX data or angle-differential data.

3.1 Bismuth

As shown in Fig.EF-2, experimental EDX-in-CMS spectrum has three peaks obviously resolved in the region of 9-15 MeV, and has additional structure in the 6-9 MeV region. The peak-a corresponds to elastic scattering, while peak-b and peak-c correspond to the 2.49 MeV and 4.30 MeV states of discrete inelastic scattering which may be collective excitations. Since the treatment of inelastic scattering in ENDL-86 for these energy regions is done with the pre-equilibrium process only, significant underestimation of ENDL-86 can be overcome by adding inelastic components of direct process. In the energy region lower than ca. 6.5 MeV where ^{209}Bi(n,2n) neutrons are dominant, the experimental spectrum is much softer than that of ENDL-86. A trial calculation with GNASH86[8] has shown[3] that we can reproduce the experimental spectrum if we use a-parameter and Kalbach constant differed from empirically expected ones.

From double differential data shown in Fig.DF-1 through Fig.DF-15, we notice that neutron emission by ^{209}Bi(n,2n), in the 0-6.5 MeV region, is significantly enhanced in forward angles, compared with that of ENDL-86 which shows good agreement with the experiment in forward angles and significantly underestimates in backward angles. The angular dependence of neutron emission from preequilibrium process shall be further investigated. Discrepancy by ENDL-86 in the 7-13 MeV region is of course much more distinct in DDX data, due to the forward-peaking tendency of direct inelastic scattering which is clearly visible in experimental data.

Differential elastic scattering cross sections are shown in Fig.AF-1. Very good agreement between the present experiment and the ENDL-86 evaluation is seen for forward angles up to ca. 50°, beyond which however the experimental points become significantly smaller than the ENDL-86 curve although the fluctuating pattern is almost same between the two. Differential cross sections for two resolved discrete inelastic scatterings are shown in Fig. AF-2. The forward peaking tendencies are obvious for these two states. Analysis by a DWBA or coupled-channel code is expected.

Differential neutron emission cross sections of ^{209}Bi(n,2n) were deduced by integrating DDX spectrum in the energy region of 0-6.5 MeV. The result is shown in Fig.AF-3, in comparison with that of ENDL-86 which has an isotropic distribution. The experimental data shows a slight enhancement of neutron emission in forward angles. This forward-enhancement can hardly be explained by theory. However, one of two neutrons from

^{209}Bi(n,2n) reaction might be emitted in early stage of neutron-nucleus interaction.

3.2 Boron-10

In Fig.EF-4 is shown angle-integrated neutron emission spectrum in the center-of-mass system, in comparison with that of JENDL-3T[5]. Denoted peaks in the figure correspond to the elastic (a), the 3.59 MeV state (b) and the 6.03 MeV state (c), sum peak of 5,92, 6.03 and 6.13 MeV states, inelastic scattering. Between a and b, sum peak of the 1.74 and 2.16 MeV states is seen as a shoulder. Between b and c, sum peak of the 4.775 and 5.165 MeV states is observed. The JENDL-3T evaluation reproduces overall spectrum, though significant underestimations are seen in the low energy region of 1-3 MeV as well as in the high energy region of 8-11 MeV. In the energy region of 1-5 MeV, experimental spectrum is monotonously continuous, in contrast with the fluctuating structure of JENDL-3T which comes from many pseudo-levels assumed in the evaluation.

DDX data are shown in Fig.DF-16 through Fig.DF-31. Underestimation of JENDL-3T in the high energy region of 9-13 MeV is seen in forward angles of 15°, 20°, 30° and 40°, while satisfactory agreement is seen in larger angles than 50°. Similarly, underestimation of JENDL-3T in the low energy region of 1-5 MeV is observed in the forward angle range of 15°- 80°, and agreement becomes better in more backward angles than 90°. Consequently, we can state that the JENDL-3T evaluation underestimates the forward-enhancement of neutron emission in these energy regions. Similar tendency has been reported[9, 10] in the comparison with DDX data by Baba[9]. The present experimental data agree as a whole with those by Baba, though energy resolution and statistics are much better for the present experiment. DDX data by Drosg[11] go higher than the present data, in the 1-3 MeV region and their discrete peaks are more broadened[10].

In Fig.AF-4 are shown differential elastic scattering cross sections at En = 14.1 MeV, for ^{10}B. Relatively good agreement is obtained between the present data and JENDL-3T, as a whole. However, JENDL-3T slightly overestimates the experiment in the 15-40° range, while it underestimates around 60° and in the 120°-160° range. In Fig.AF-5 are shown differential cross sections for the most prominent discrete peak (5.9 to 7 MeV states) of inelastic scattering, in comparison with JENDL-3T. Good agreement is seen in the intermediate angles, while in forward and backward angles the JENDL-3T evaluation considerably overestimates the present data.

3.3 Boron-11

Angle-integrated neutron emission spectrum is shown in Fig.EF-6, in comparison with that of JENDL-3T. Six peaks are resolved in the experimental spectrum as denoted with a, b, c, d, e and f, corresponding to the elastic scattering, the 2.125 MeV state inelastic scattering, the sum-peak of 4.445 to 5.021 MeV state inelastic scattering, the sum-peak of 6.743 to 6.793 MeV state inelastic scattering, the 7.978 MeV state inelastic scattering and the sum-peak of 8.559 to 9.275 MeV state inelastic scattering, respectively. Angle-differential cross sections are given for these six resolved states, in Tables 3-1 and 3-2.

As shown in Fig.EF-6, the JENDL-3T evaluation reproduces the present data very well for three peaks (a, b and c) in the 6-13 MeV region, though disagreements between peaks can be attributed to the tail of energy resolution function of experiment[2]. In the low energy region of 0 - 6 MeV, disagreement is obvious on the contrary. The JENDL-3T overevaluates partial cross sections for the 6.743 - 6.793 states, by ca. twice. In the experiment, additional two peaks (e and f) can be resolved and these are not considered in JENDL-3T. If we compare Fig.EF-6 and Fig.EF-5, we notice that such high energy-state excitations do not appear for boron-10, but do appear for boron-11. This high energy-state excitations for boron-11 is hardly seen in the data by Drosg[11], but is appearing in the data by Baba[9].

DDX data are shown in Fig.DF-32 through Fig.DF-47, in comparison with those of JENDL-3T. Underestimation of JENDL-3T is significant in the low energy region of 0 - ca. 6 MeV, for forward angles (15° to 60°), while agreement in average is seen in backward angles though spectral shape is different due to neglection of the high energy-state excitations in JENDL-3T. Similar tendencies are seen in comparison with the data by Drosg[11] and Baba[9], as shown in Ref.10. At elastic scattering peaks for 60°, 70°, 110°, 120°, 127.9° and 140°, drastic underestimations of JENDL-3T are seen. This is discussed in the following for angle-differential cross sections. We can say that the present data are obtained very successfully from viewpoints of energy resolution and statistics.

Angle-differential cross sections for six resolved discrete states are shown in Fig.AF-6 through Fig.AF-9. Differential elastic scattering cross sections are shown in Fig.AF-6, in comparison with JENDL-3T. We find large disagreement in the whole angle range. The JENDL-3T evaluation under-

estimates the present data at larger angles than ca. 50°, drastically, and overestimates at forward angles. Optical potentials in JENDL-3T shall be readjusted. In Fig.AF-7 through Fig.AF-9 are shown differential inelastic scattering cross sections for five resolved states. For the 2.125 MeV state, the present data show much more forward-enhancement than that of JENDL-3T. For the 4.445 - 5.021 MeV state, however, agreement is good. And for the 6.743 - 6.793 state the JENDL-3T curve again underestimates the forward-enhancement of experiment. For the 7.978 MeV state, significant enhancement in forward angles is not seen. However, for the 8.559 - 9.275 MeV states, considerable forward enhancement is observed.

4. SUMMARY

Double differential neutron emission cross sections at En = 14.1 MeV for 15 - 16 angle-points have been measured with satisfactory energy resolution and counting statistics, for ^{209}Bi, ^{10}B and ^{11}B. Angle-integrated neutron emission spectra in either CMS or LAB-system have been deduced. Within the attained energy resolution, some of discrete excited states by elastic and inelastic scattering could be resolved. Tabulated numerical data and graphs are given in this report for all of these data.

Obtained data are of huge amount. To see a trend of data, however, angle-integrated spectra can be first compared with evaluated nuclear data or theoretical calculations. Then we can look in deep by comparisons for double differential and angle-differential data. This kind of comparison and discussion has been done in this report, using ENDL-86 for Bi and JENDL-3T for boron isotopes as references.

For ^{209}Bi(n,2n) reaction, the present experiment has given much softer spectrum of emitted neutrons than that of ENDL-86. Considerable enhancement of neutron emission in forward angles shall be further analyzed. Resolved two states of inelastic scattering shall be added in future evaluations including JENDL-3, using calculations by the direct reaction theory. For boron-10, the JENDL-3T evaluation is relatively successful though underestimations are seen in secondary energy regions of 1-5 and 8-11 MeV. For boron-11, JENDL-3T has shown a drastic disagreement with the present data for elastic scattering and low energy part (high excited states) of inelastic scattering neutrons.

estimates the present data at larger angles than ca. 50°, drastically, and overestimates at forward angles. Optical potentials in JENDL-3T shall be readjusted. In Fig.AF-7 through Fig.AF-9 are shown differential inelastic scattering cross sections for five resolved states. For the 2.125 MeV state, the present data show much more forward-enhancement than that of JENDL-3T. For the 4.445 - 5.021 MeV state, however, agreement is good. And for the 6.743 - 6.793 state the JENDL-3T curve again underestimates the forward-enhancement of experiment. For the 7.978 MeV state, significant enhancement in forward angles is not seen. However, for the 8.559 - 9.275 MeV states, considerable forward enhancement is observed.

4. SUMMARY

Double differential neutron emission cross sections at En = 14.1 MeV for 15 - 16 angle-points have been measured with satisfactory energy resolution and counting statistics, for ^{209}Bi, ^{10}B and ^{11}B. Angle-integrated neutron emission spectra in either CMS or LAB-system have been deduced. Within the attained energy resolution, some of discrete excited states by elastic and inelastic scattering could be resolved. Tabulated numerical data and graphs are given in this report for all of these data.

Obtained data are of huge amount. To see a trend of data, however, angle-integrated spectra can be first compared with evaluated nuclear data or theoretical calculations. Then we can look in deep by comparisons for double differential and angle-differential data. This kind of comparison and discussion has been done in this report, using ENDL-86 for Bi and JENDL-3T for boron isotopes as references.

For ^{209}Bi(n,2n) reaction, the present experiment has given much softer spectrum of emitted neutrons than that of ENDL-86. Considerable enhancement of neutron emission in forward angles shall be further analyzed. Resolved two states of inelastic scattering shall be added in future evaluations including JENDL-3, using calculations by the direct reaction theory. For boron-10, the JENDL-3T evaluation is relatively successful though underestimations are seen in secondary energy regions of 1-5 and 8-11 MeV. For boron-11, JENDL-3T has shown a drastic disagreement with the present data for elastic scattering and low energy part (high excited states) of inelastic scattering neutrons.

Acknowledgment

The present work has been financially supported by the 1987 Research-in-Trust from the Japan Atomic Energy Research Institute (JAERI). The authors are greately appreciate to Drs. S. Igarasi and T. Asami and other members of the JAERI Nuclear Data Center. They are also grateful to the operation crew of OKTAVIAN, Messrs. J. Datemichi and S. Yoshida.

References

1) Cheng, E. T., GA-A18152 (1985)
2) Takahashi, A., et al., J. Nucl. Sci. Technol., 25, 215-232, (1988)
3) idem., 'Angle-integrated neutron emission spectra at 14 MeV for Be, C, F, Mg, Al, Si, V, Fe, Cr, Cu, Pb and Bi', Proc. Seminar on Nuclear Data, Nov. 1987, Tokai, Japan, to be published in JAERI-M.
4) Howerton, R. J., UCRL-50400 Vol.25, (1983), and private communication.
5) JENDL Compilation Group (Nuclear Data Center, JAERI), JENDL-3T, private communication.
6) Ichimura, E., Takahashi, A., OKTAVIAN Rep. A-87-02, Osaka Univ., (1987)
7) Yamamoto, J., et al., J. Nucl. Sci. Technol., 19, 276-288, (1982)
8) Yamamuro, N., JAERI-memo 61-260, and private communication.
9) Baba, M., et al., Rad. Eff., 92, 223, (1986)
10) Fukahori, M., Tasaki, I., JAERI-memo 62-453, (1988)
11) Drosg, M., et al., Rad. Eff., 92, 145, (1986)

Acknowledgment

The present work has been financially supported by the 1987 Research-in-Trust from the Japan Atomic Energy Research Institute (JAERI). The authors are greately appreciate to Drs. S. Igarasi and T. Asami and other members of the JAERI Nuclear Data Center. They are also grateful to the operation crew of OKTAVIAN, Messrs. J. Datemichi and S. Yoshida.

References

1) Cheng, E. T., GA-A18152 (1985)
2) Takahashi, A., et al., J. Nucl. Sci. Technol., 25, 215-232, (1988)
3) idem., 'Angle-integrated neutron emission spectra at 14 MeV for Be, C, F, Mg, Al, Si, V, Fe, Cr, Cu, Pb and Bi', Proc. Seminar on Nuclear Data, Nov. 1987, Tokai, Japan, to be published in JAERI-M.
4) Howerton, R. J., UCRL-50400 Vol.25, (1983), and private communication.
5) JENDL Compilation Group (Nuclear Data Center, JAERI), JENDL-3T, private communication.
6) Ichimura, E., Takahashi, A., OKTAVIAN Rep. A-87-02, Osaka Univ., (1987)
7) Yamamoto, J., et al., J. Nucl. Sci. Technol., 19, 276-288, (1982)
8) Yamamuro, N., JAERI-memo 61-260, and private communication.
9) Baba, M., et al., Rad. Eff., 92, 223, (1986)
10) Fukahori, M., Tasaki, I., JAERI-memo 62-453, (1988)
11) Drosg, M., et al., Rad. Eff., 92, 145, (1986)

Table 1 Partial differential cross sections for Bismuth at 14.1MeV

θ_{LAB} (deg)	elastic		Q=-2.492 MeV		Q= -4.3 MeV		(n, 2n)	
	dσ/dΩ(b/sr)	error	dσ/dΩ(b/sr)	error	dσ/dΩ(b/sr)	error	dσ/dΩ(b/sr)	error
15	3.11E+0	9.3E-2	3.97E-2	2.0E-3	2.24E-2	1.1E-3	4.02E-1	1.2E-2
20	7.95E-1	2.4E-2	1.80E-2	5.4E-4	1.32E-2	4.0E-4	3.77E-1	1.1E-2
30	2.57E-1	7.7E-3	1.15E-2	3.5E-4	1.38E-2	4.1E-4	3.74E-1	1.1E-2
40	4.40E-1	1.3E-3	1.16E-2	3.5E-4	1.01E-2	3.0E-4	3.54E-1	1.1E-2
50	1.43E-1	4.3E-3	1.04E-2	3.1E-4	1.00E-2	3.0E-4	3.43E-1	1.0E-2
60	5.73E-2	1.8E-3	7.08E-3	2.1E-4	7.43E-3	2.2E-4	3.35E-1	1.0E-2
70	7.66E-2	2.3E-3	5.12E-3	1.5E-4	6.84E-3	2.1E-4	3.24E-1	9.7E-3
80	3.22E-2	9.7E-4	4.54E-3	1.4E-4	4.40E-3	1.3E-4	3.39E-1	1.0E-2
90	1.08E-2	3.2E-4	4.51E-3	1.4E-4	3.12E-3	9.4E-5	3.28E-1	9.8E-3
100	2.35E-2	7.0E-4	3.57E-3	1.1E-4	4.46E-3	1.3E-4	3.23E-1	9.7E-3
110	1.29E-2	3.8E-4	2.53E-3	7.6E-5	2.48E-3	7.4E-5	2.56E-1	7.7E-3
120	5.82E-3	1.7E-4	2.41E-3	7.2E-5	2.06E-3	6.2E-5	2.79E-1	8.4E-3
130	5.84E-3	1.8E-4	2.31E-3	6.9E-5	———	———	2.52E-1	7.6E-3
140	8.11E-3	2.4E-4	1.18E-3	3.5E-5	1.99E-3	1.0E-4	2.80E-1	8.4E-3
150	5.57E-3	1.7E-4	1.69E-3	5.1E-5	———	———	2.33E-1	7.0E-3
σ_{Total} (barn)	———	———	6.91E-2	2.1E-3	6.71E-2	3.4E-3	3.84E+0	1.2E-1

Table 2 Partial differential cross sections for Boron-10 at 14.1MeV

θ_{LAB} (deg)	elastic		Q=-5.92~7.00 MeV	
	$d\sigma/d\Omega$(b/sr)	error	$d\sigma/d\Omega$(b/sr)	error
15	6.99E-1	2.1E-2	1.54E-2	8.8E-4
20	5.64E-1	1.7E-2	1.35E-2	5.6E-4
30	3.31E-1	9.9E-3	1.34E-2	4.0E-4
40	1.50E-1	4.5E-3	1.52E-2	4.6E-4
50	6.51E-2	2.0E-3	1.30E-2	3.9E-4
60	2.52E-2	7.5E-4	9.05E-3	2.7E-4
70	2.10E-2	6.3E-4	7.58E-3	2.3E-4
80	2.40E-2	7.2E-4	6.42E-3	1.9E-4
90	2.56E-2	7.7E-4	6.38E-3	1.9E-4
100	2.46E-2	7.4E-4	5.34E-3	1.6E-4
110	1.90E-2	5.7E-4	5.77E-3	1.7E-4
120	1.27E-3	3.8E-4	4.69E-3	1.5E-4
130	9.21E-3	2.8E-4	4.66E-3	1.4E-4
140	5.72E-3	1.7E-4	4.42E-3	1.5E-4
150	4.54E-3	1.4E-4	3.34E-3	1.9E-4
160	6.57E-3	2.0E-4	3.87E-3	3.5E-4
σ_{Total} (barn)	9.09E-1	2.7E-2	8.99E-2	2.7E-3

Table 3 Partial differential cross sections for Boron-11 at 14.1MeV

θ_{LAB} (deg)	elastic		Q=-2.125 MeV		Q= -4.445~5.021 MeV		Q= -6.743~6.793 MeV	
	$d\sigma/d\Omega$(b/sr)	error	$d\sigma/d\Omega$(b/sr)	error	$d\sigma/d\Omega$(b/sr)	error	$d\sigma/d\Omega$(b/sr)	error
15	7.39E-1	2.2E-2	1.74E-2	8.7E-4	2.26E-2	7.0E-4	1.37E-2	5.7E-4
20	6.00E-1	1.8E-2	1.66E-2	8.3E-4	2.07E-2	6.2E-4	1.33E-2	4.1E-4
30	3.61E-1	1.1E-2	1.11E-2	5.5E-4	1.89E-2	5.7E-4	1.22E-2	3.7E-4
40	1.76E-1	5.3E-3	7.97E-3	4.0E-4	1.51E-2	4.5E-4	1.06E-2	3.2E-4
52.1	5.47E-2	1.6E-3	4.78E-3	2.4E-4	1.20E-2	3.6E-4	7.55E-3	2.3E-4
60	2.28E-2	6.9E-4	3.30E-3	1.7E-4	1.01E-2	3.1E-4	6.11E-3	1.8E-4
70	2.30E-2	6.9E-4	2.39E-3	1.2E-4	8.49E-3	2.5E-4	4.96E-3	1.5E-4
80	2.98E-2	9.0E-4	1.60E-3	8.8E-5	7.23E-3	2.2E-4	4.74E-3	1.4E-4
90	3.21E-2	9.6E-4	1.73E-3	9.9E-5	7.20E-3	2.2E-4	4.67E-3	1.4E-4
100	3.22E-2	9.7E-4	1.73E-3	1.0E-4	6.78E-3	2.0E-4	4.69E-3	1.4E-4
110	2.68E-2	8.0E-4	1.61E-3	9.1E-5	6.40E-3	1.9E-4	4.41E-3	1.3E-4
120	1.73E-2	5.2E-4	1.76E-3	9.5E-5	5.84E-3	1.8E-4	4.32E-3	1.3E-3
127.9	1.09E-2	3.3E-4	1.68E-3	1.0E-4	5.27E-3	1.6E-4	4.68E-3	1.4E-4
140	5.99E-3	1.8E-4	2.03E-3	1.0E-4	5.64E-3	1.7E-4	5.17E-3	1.5E-4
150	6.70E-3	2.0E-4	2.29E-3	1.5E-4	6.02E-3	1.9E-4	4.47E-3	1.6E-4
160	7.95E-3	3.3E-4	2.40E-3	2.9E-4	6.96E-3	3.7E-4	4.49E-3	2.9E-4
σ_{Total} (barn)	9.89E-1	3.0E-2	4.57E-2	2.7E-3	1.14E-1	3.4E-3	7.60E-2	2.3E-3

Table 3 (continued)

θ_{LAB} (deg)	Q＝-7.978 MeV		Q= -8.559~9.275 MeV	
	$d\sigma/d\Omega$(b/sr)	error	$d\sigma/d\Omega$(b/sr)	error
15	7.06E-4	1.7E-4	7.11E-3	3.8E-4
20	6.441-4	1.2E-4	6.77E-3	2.7E-4
30	1.48E-3	1.0E-4	6.00E-3	1.8E-4
40	1.84E-3	1.3E-4	5.20E-3	1.6E-4
52.1	1.94E-3	1.4E-4	5.59E-3	1.7E-4
60	1.57E-3	1.1E-4	5.04E-3	1.5E-4
70	1.50E-3	1.0E-4	4.85E-3	1.5E-4
80	1.57E-3	1.0E-4	4.12E-3	1.2E-4
90	2.07E-3	1.4E-4	3.34E-3	1.0E-4
100	1.45E-3	1.0E-4	3.27E-3	1.1E-4
110	1.37E-3	9.6E-5	2.75E-3	9.8E-5
120	1.16E-3	8.1E-5	2.16E-3	7.9E-5
127.9	9.88E-4	7.8E-5	2.07E-3	8.8E-5
140	1.35E-3	9.4E-5	2.43E-3	8.5E-5
150	9.01E-4	1.0E-4	2.57E-3	1.4E-4
160	1.48E-3	2.6E-4	2.54E-3	2.6E-4
σ_{Total} (barn)	1.82E-2	1.3E-3	4.84E-2	2.1E-3

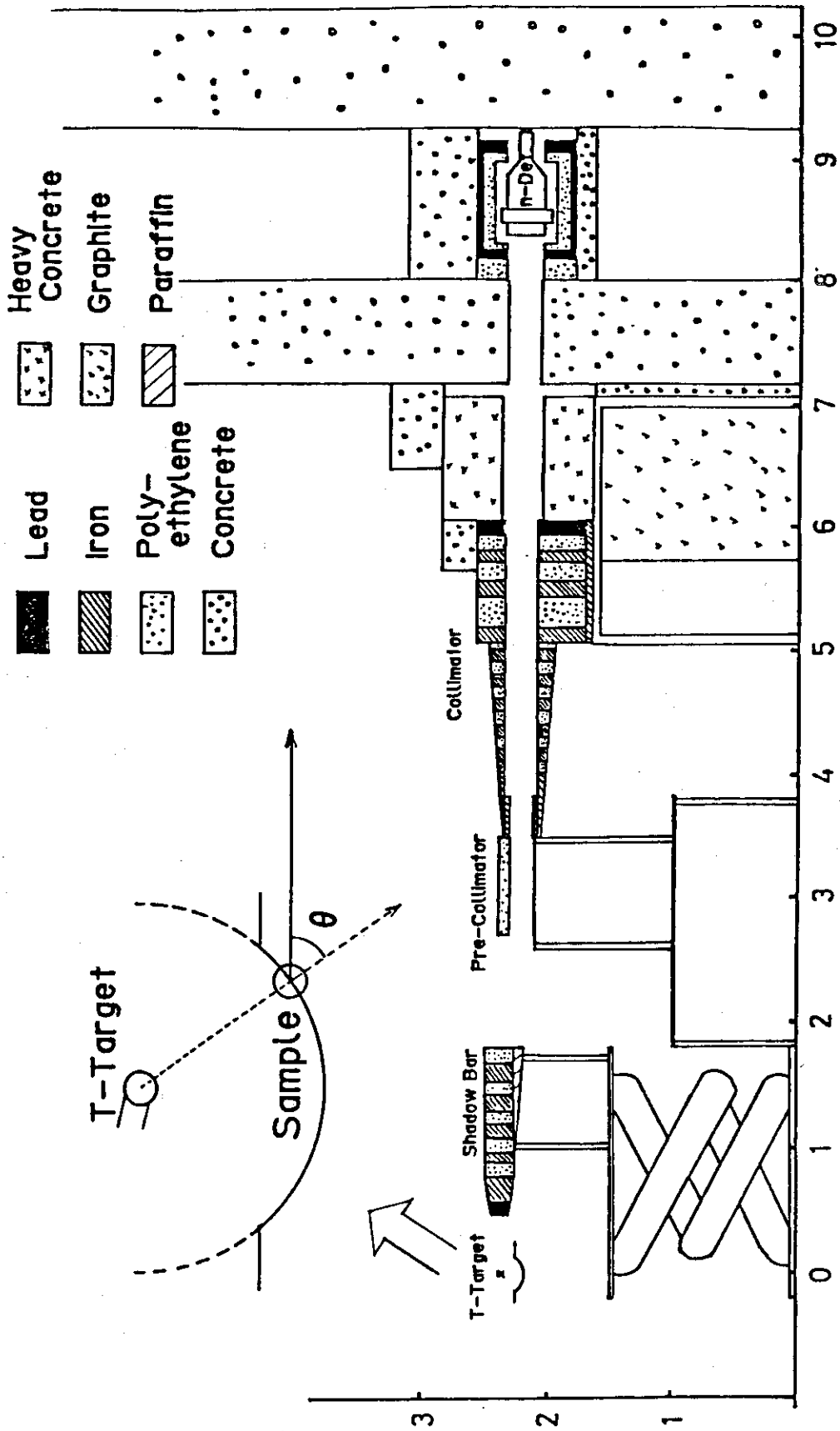

Fig.I-1 Schematic view of the neutron time-of-flight facility to measure double differential neutron emission cross sections.

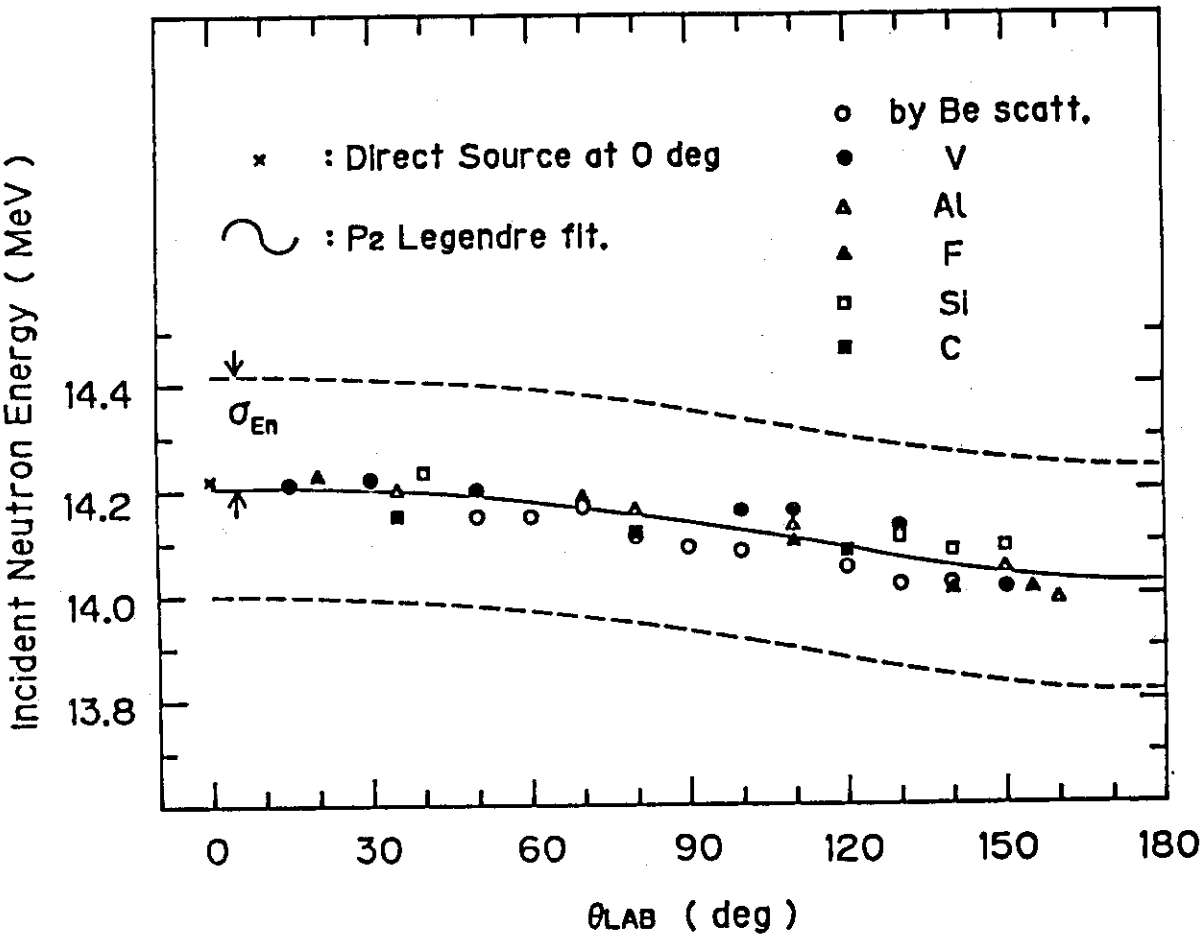

Fig.I-2 Variation of incident neutron energy with the change of scattering angle. Band of broken lines shows energy resolution.

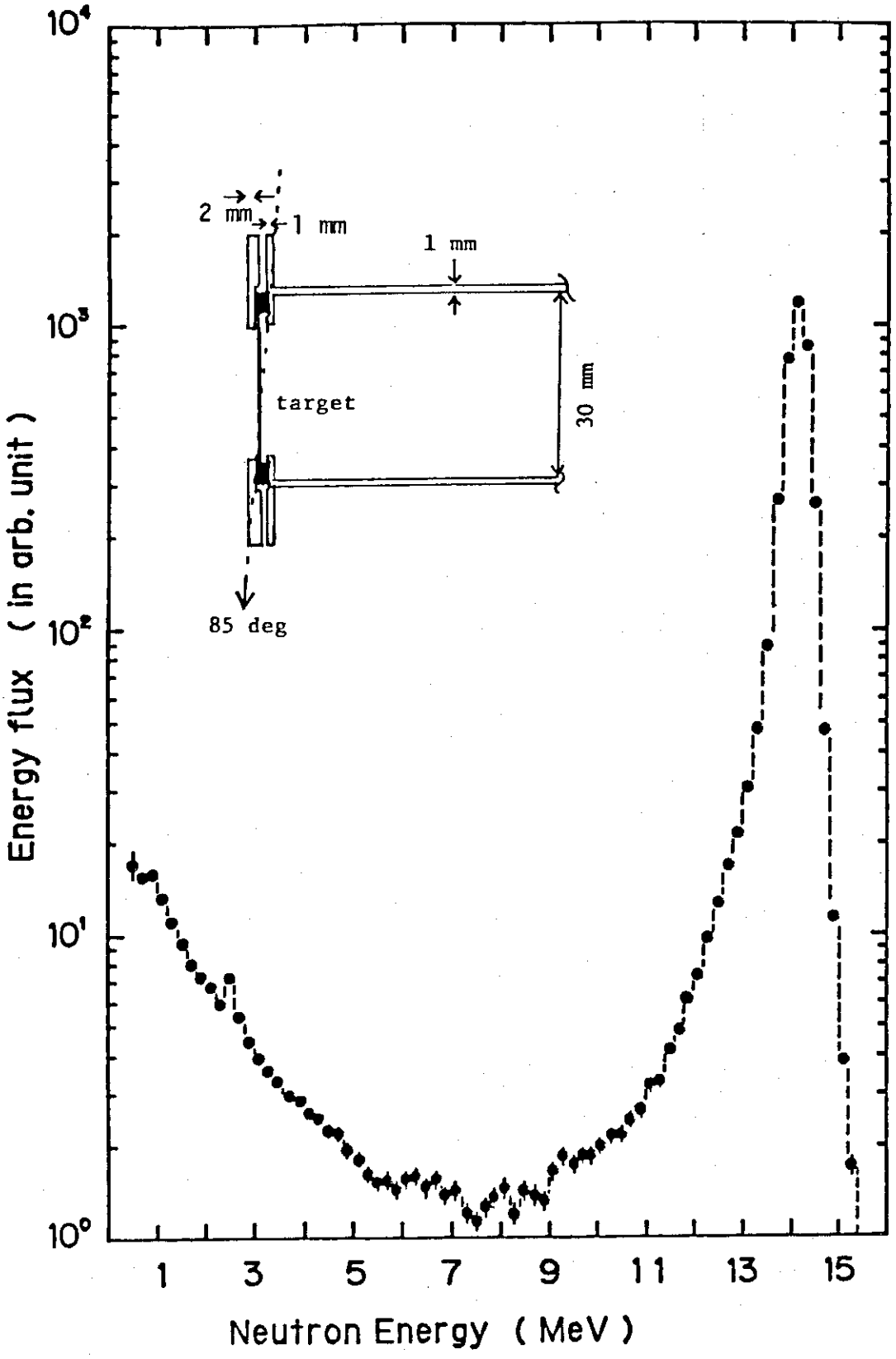

Fig.I-3 Measured flux spectrum of source neutrons of the TiT target. The insert shows the target structure.

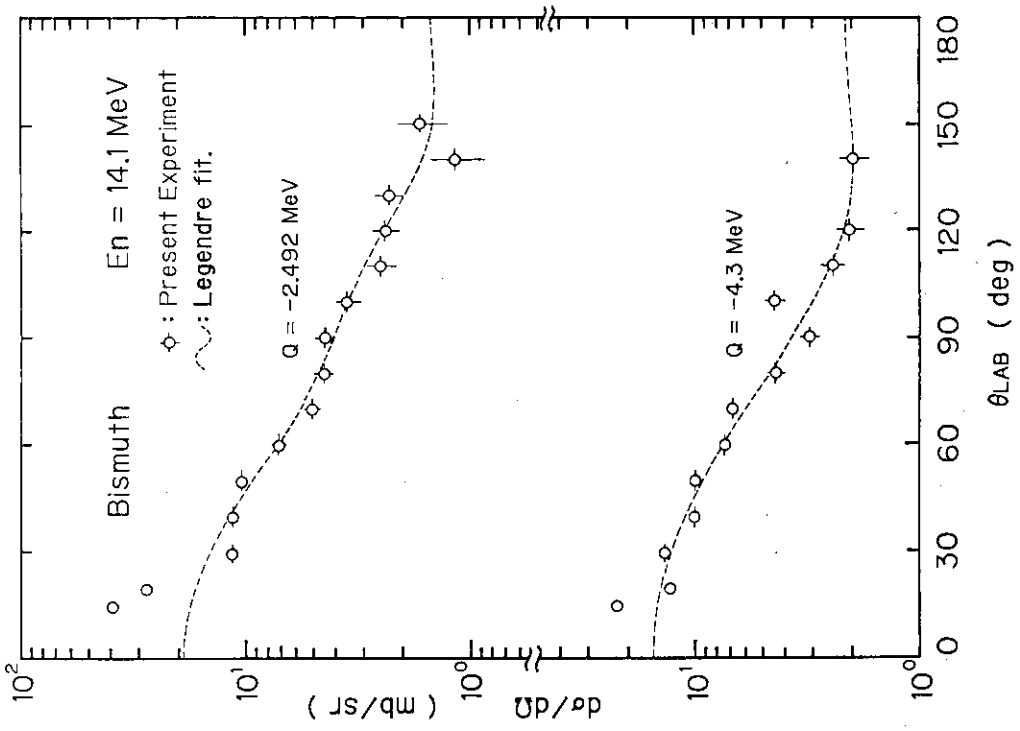

Fig.AF-2 Differential inelastic scattering cross sections for the 2.492 and 4.3 MeV states of ^{209}Bi.

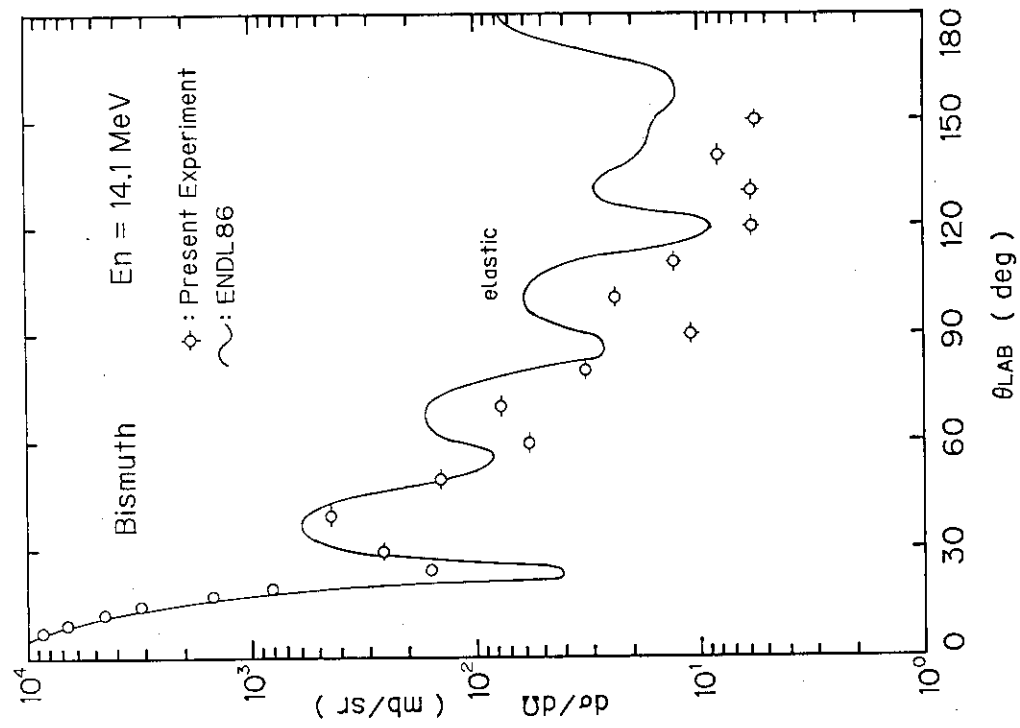

Fig.AF-1 Differential elastic scattering cross sections for ^{209}Bi, with incident neutron energy of 14.1 MeV.

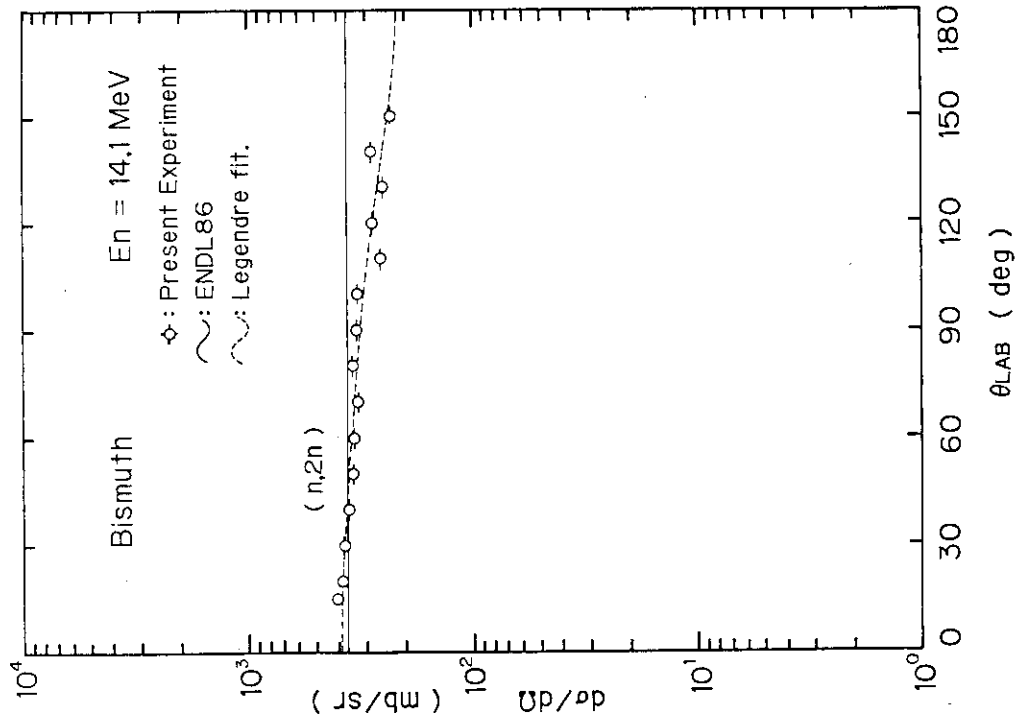

Fig.AF-3 Angular distribution of ^{209}Bi(n,2n) neutrons, i.e., differential neutron emission cross sections.

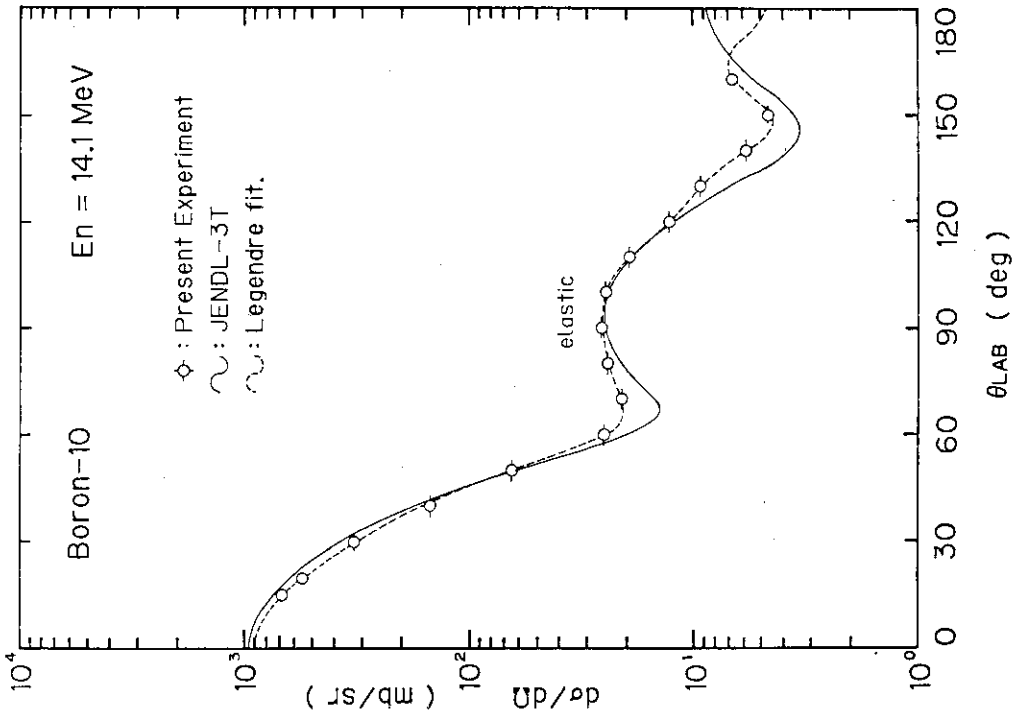

Fig.AF-4 Differential elastic scattering cross sections for ^{10}B, with incident neutron energy of 14.1 MeV.

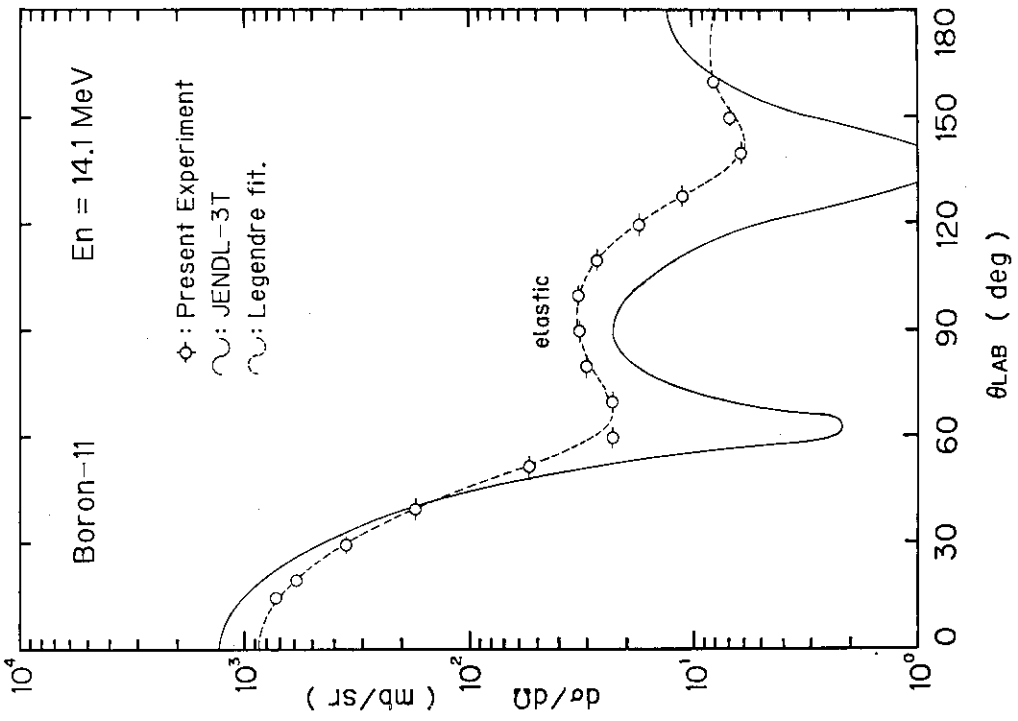

Fig.AF-6 Differential elastic scattering cross sections for ^{11}B, with incident neutron energy of 14.1 MeV.

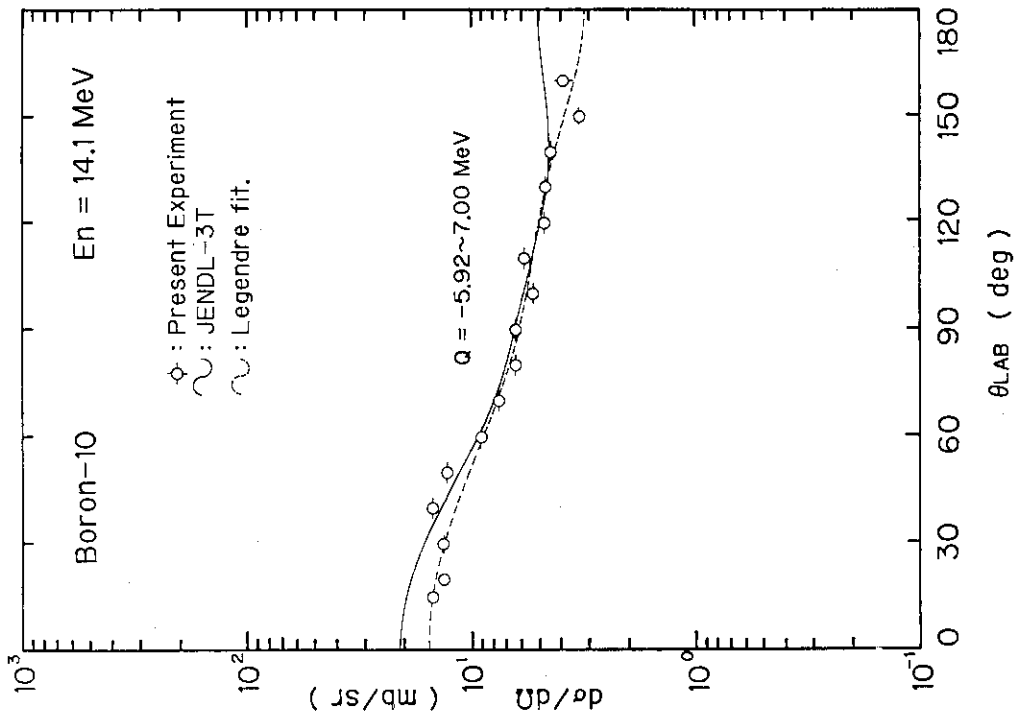

Fig.AF-5 Differential inelastic scattering cross sections for the 5.9-7 MeV state of ^{10}B, with incident neutron energy of 14.1 MeV.

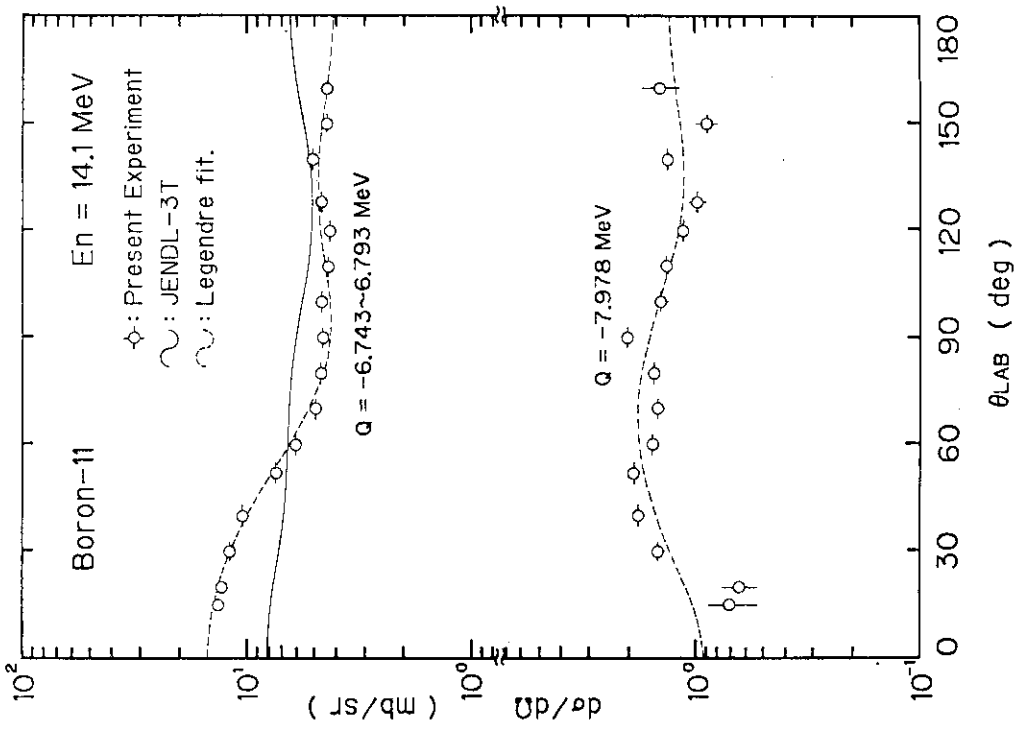

Fig.AF-8 Differential inelastic scattering cross sections for the 6.743-6.793 and 7.978 MeV states of ^{11}B, with incident neutron energy of 14.1 MeV.

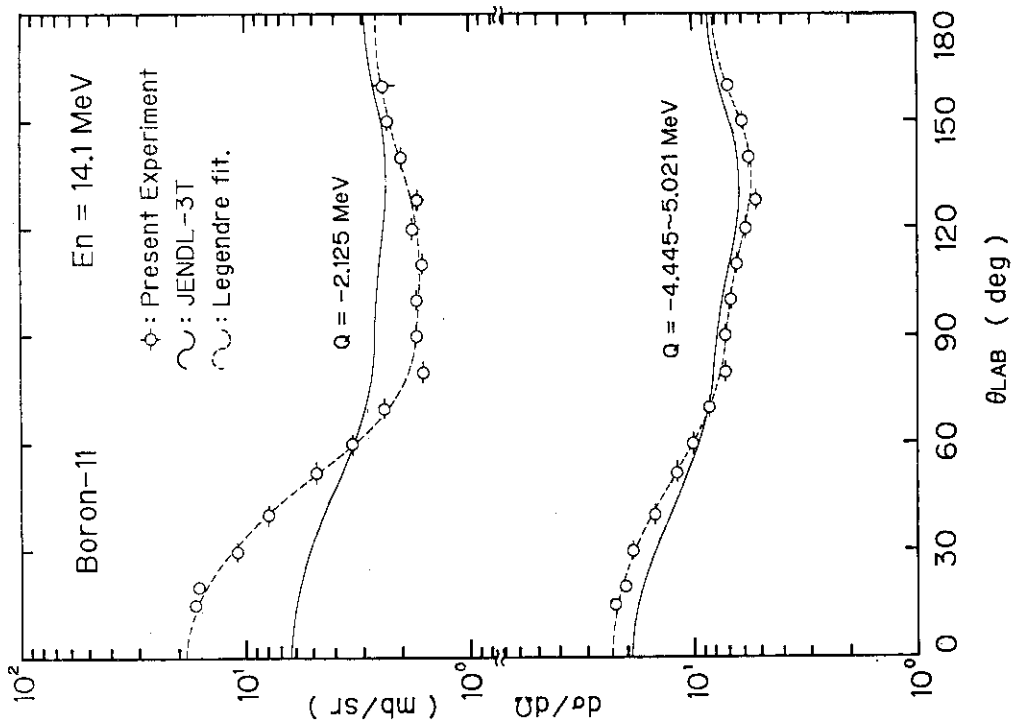

Fig.AF-7 Differential inelastic scattering cross sections for the 2.125 and 4.445-5.021 MeV states of ^{11}B, with incident neutron energy of 14.1 MeV.

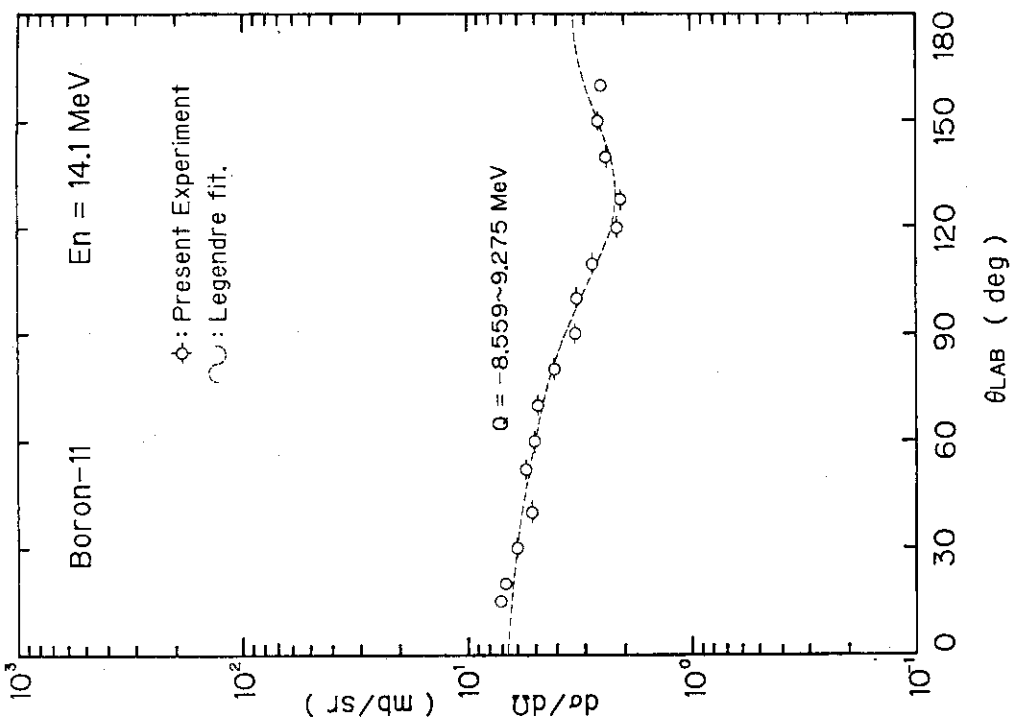

Fig.AF-9 Differential inelastic scattering cross sections for the 8.559-9.275 MeV states of ^{11}B, with incident neutron energy of 14.1 MeV.

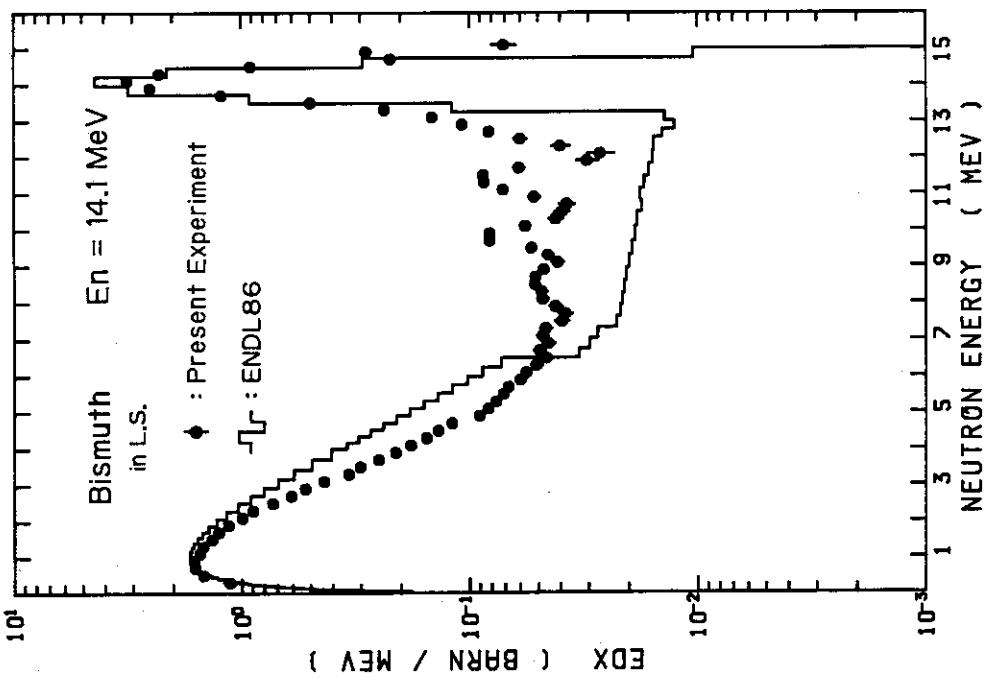

Fig.EF-1 Angle-integrated neutron emission spectra in the LAB system for ^{209}Bi, with incident neutron energy of 14.1 MeV.

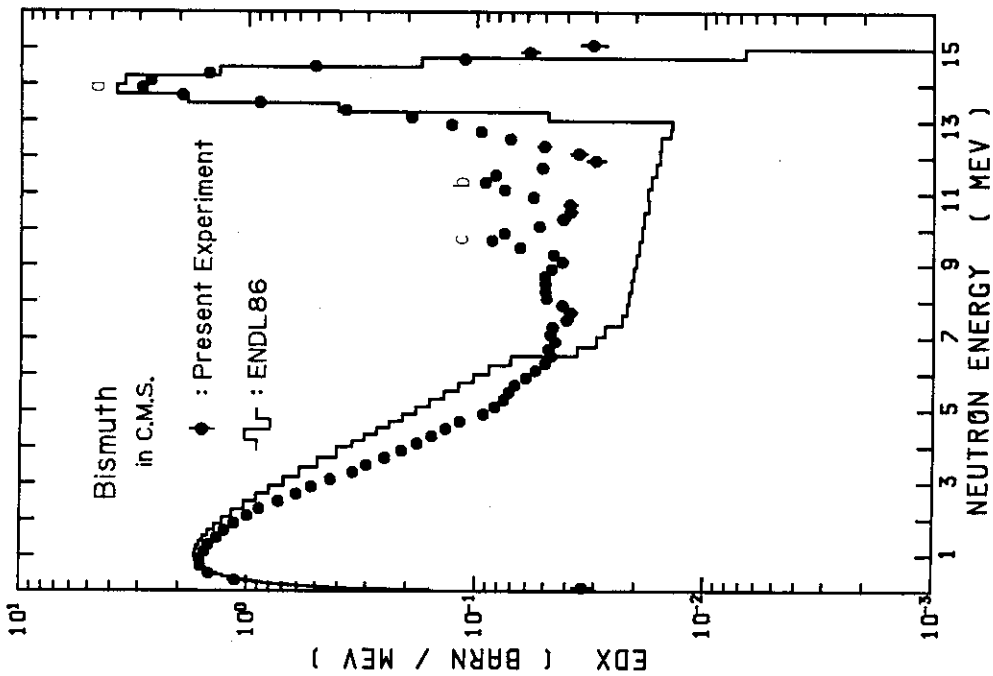

Fig.EF-2 Angle-integrated neutron emission spectra in the center-of-mass system for ^{209}Bi, with incident neutron energy of 14.1 MeV.

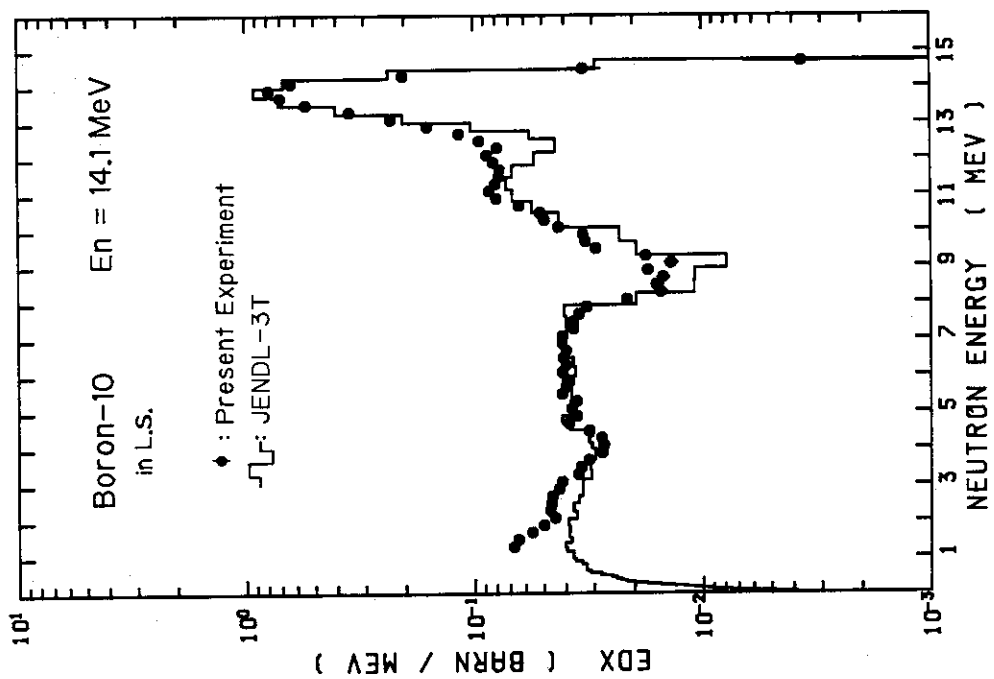

Fig.EF-3 Angle-integrated neutron emission spectra in the LAB system for ^{10}B, with incident neutron energy of 14.1 MeV.

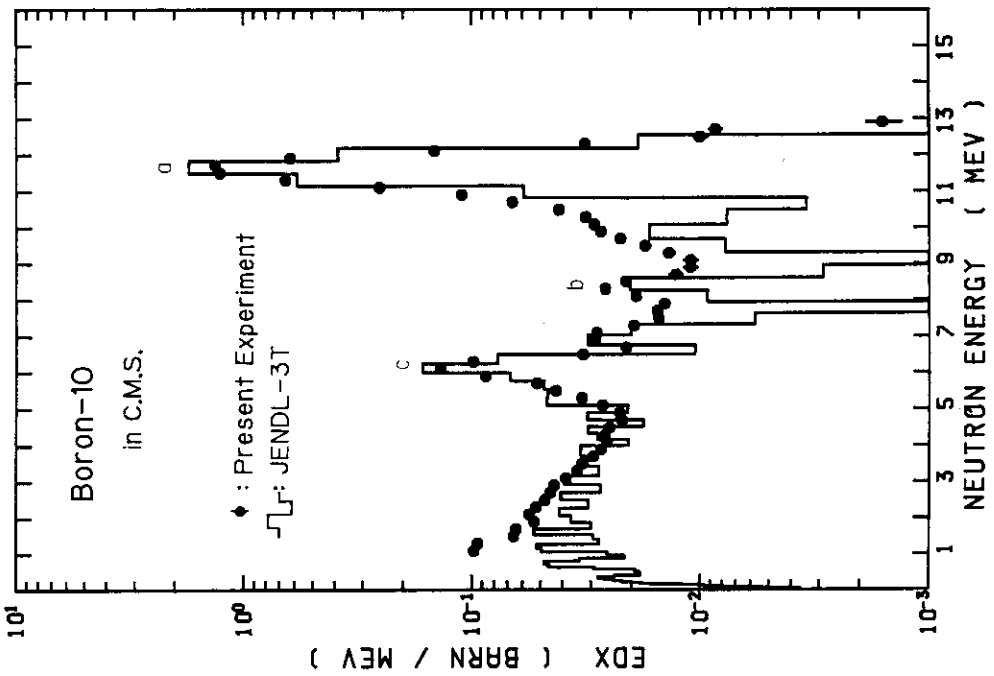

Fig.EF-4 Angle-integrated neutron emission spectra in the center-of-mass system for ^{10}B, with incident neutron energy of 14.1 MeV.

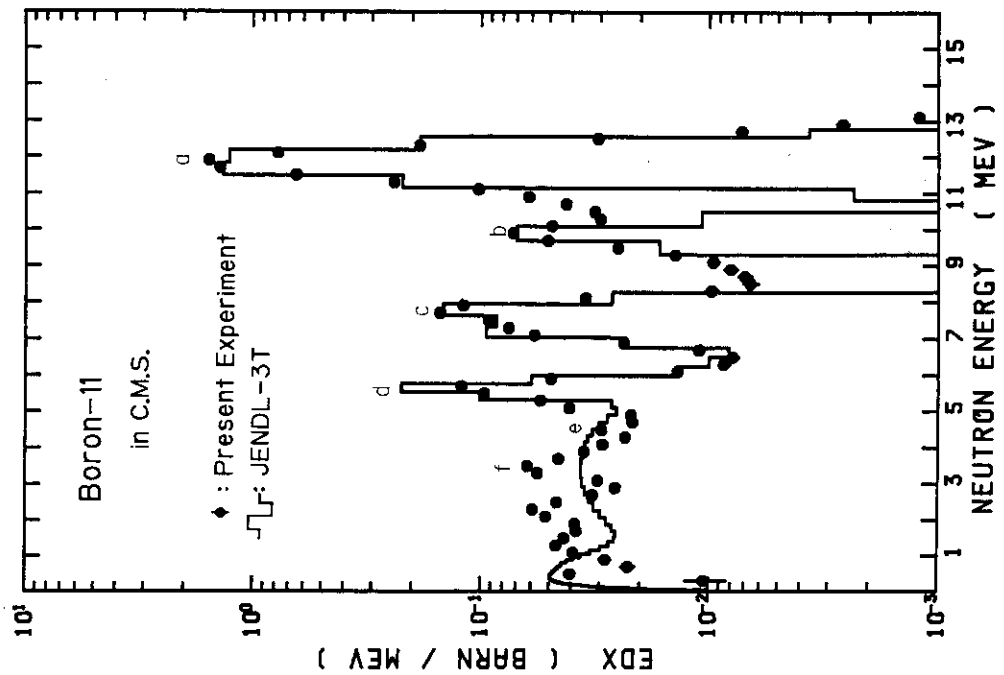

Fig.EF-6 Angle-integrated neutron emission spectra in the center-of-mass system for ^{11}B, with incident neutron energy of 14.1 MeV.

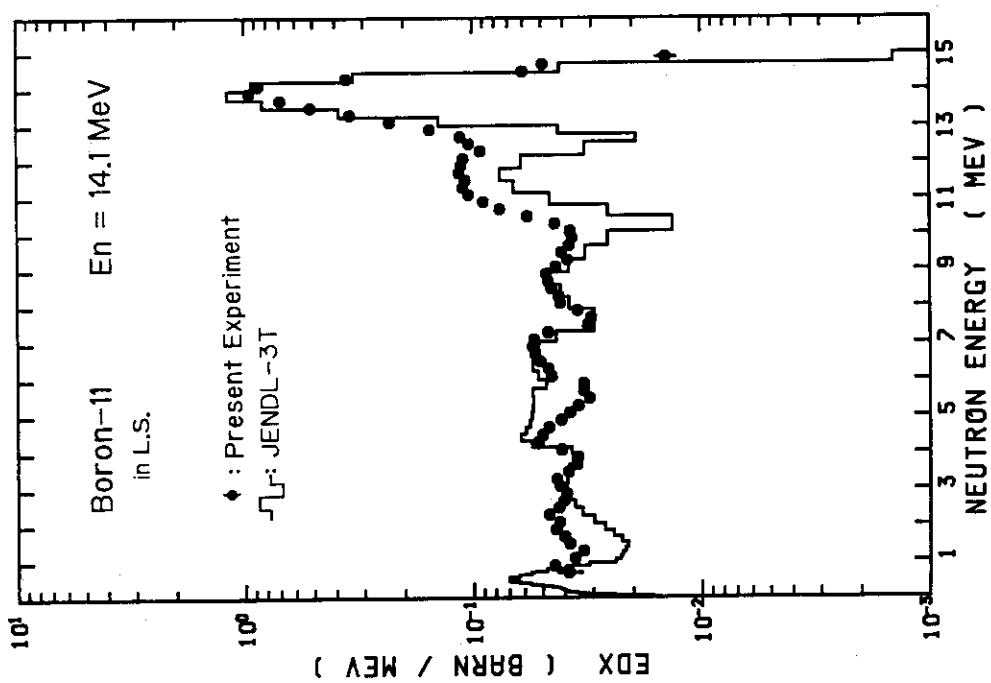

Fig.EF-5 Angle-integrated neutron emission spectra in the LAB system for ^{11}B, with incident neutron energy of 14.1 MeV.

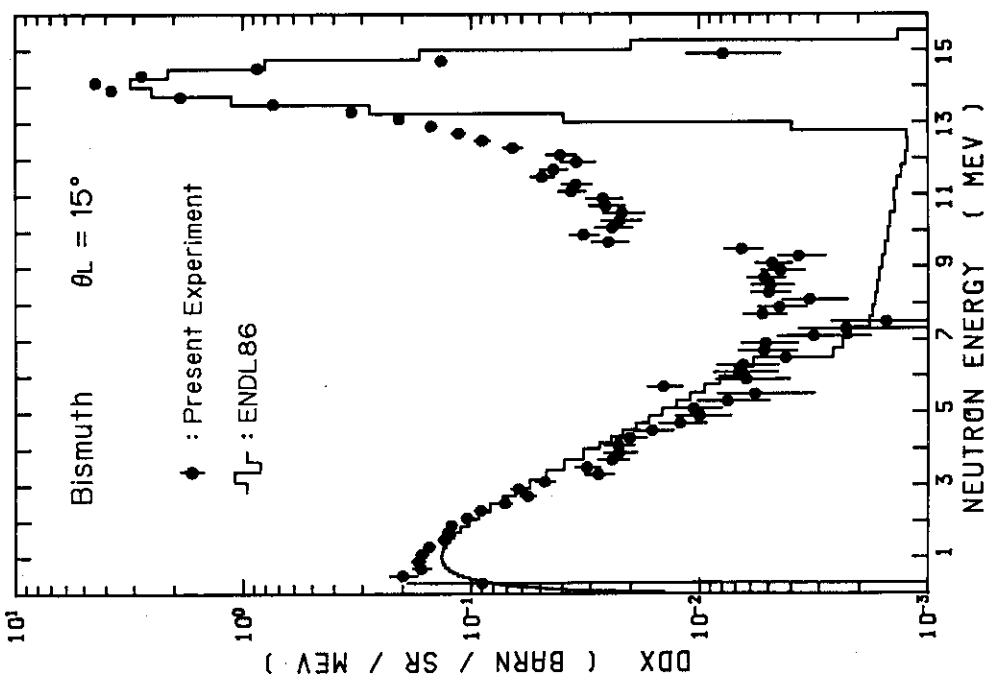

Fig.DF-1 Double differential neutron emission cross sections for ^{209}Bi, at 15°, with incident neutron energy of 14.1 MeV.

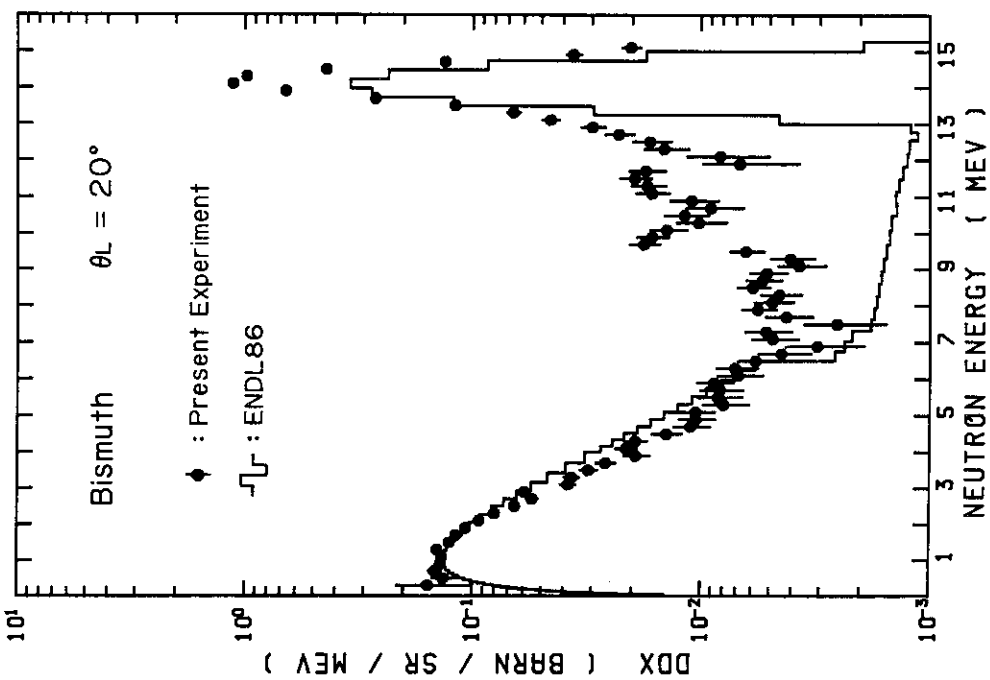

Fig.DF-2 Double differential neutron emission cross sections for ^{209}Bi, at 20°, with incident neutron energy of 14.1 MeV.

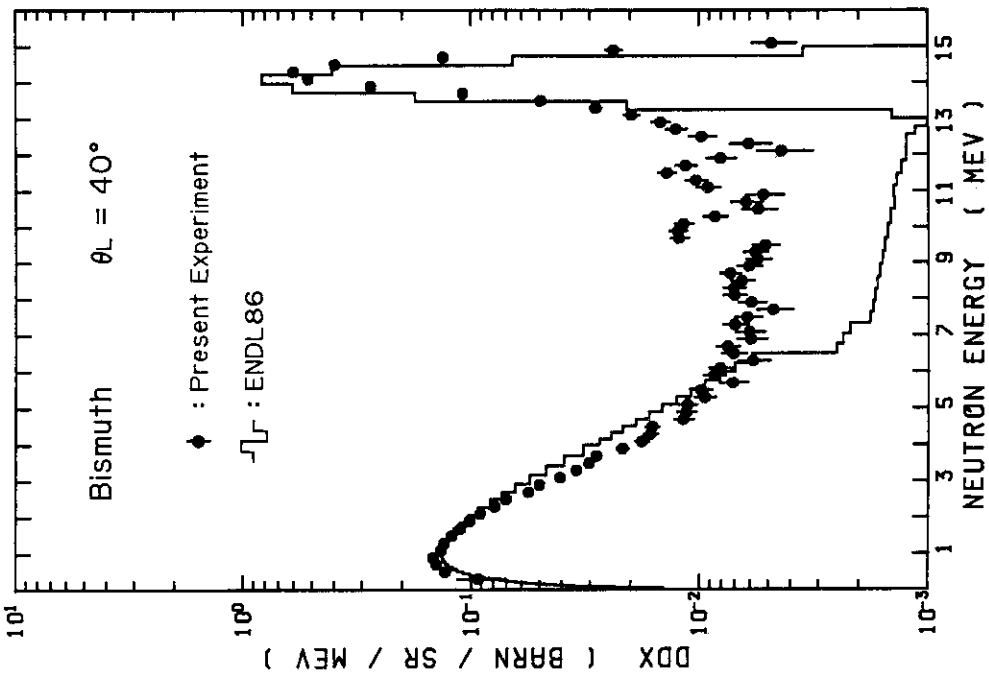

Fig.DF-4 Double differential neutron emission cross sections for ^{209}Bi, at 40°, with incident neutron energy of 14.1 MeV.

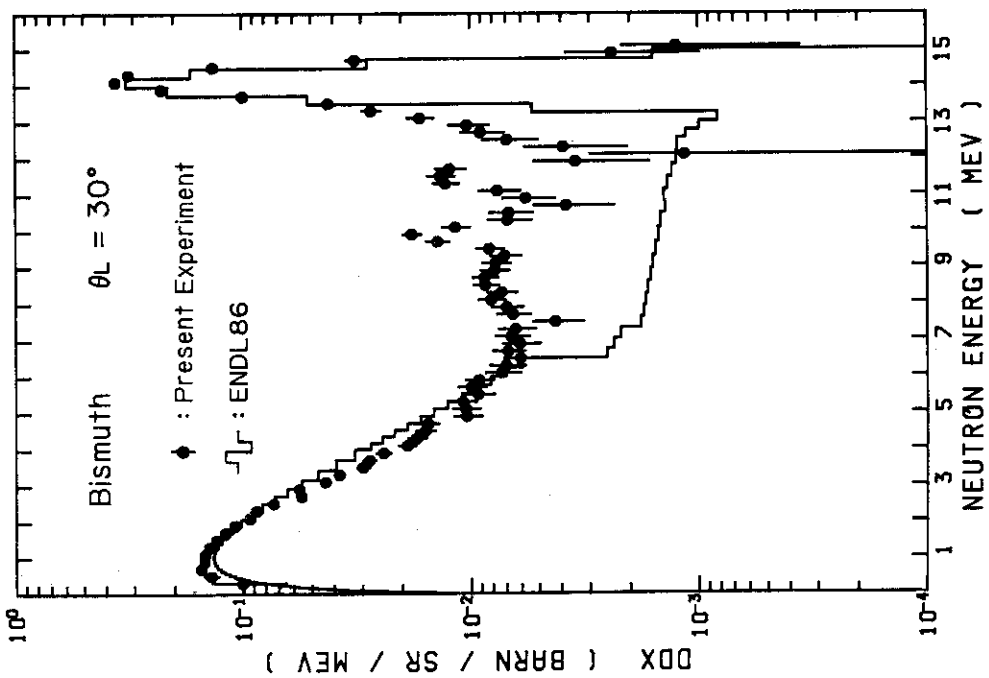

Fig.DF-3 Double differential neutron emission cross sections for ^{209}Bi, at 30°, with incident neutron energy of 14.1 MeV.

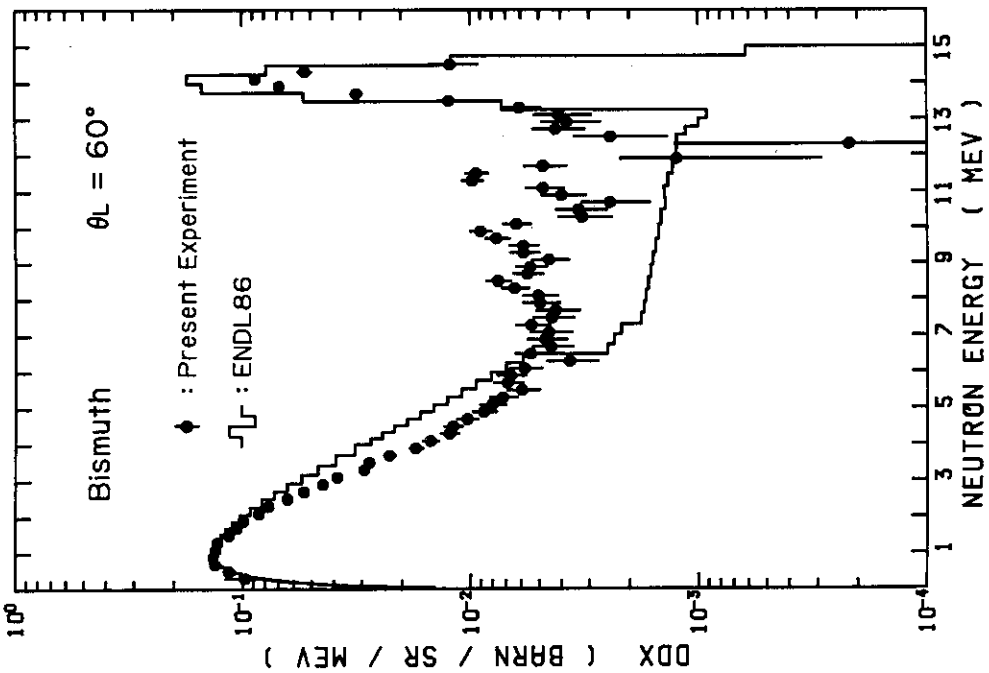

Fig.DF-6 Double differential neutron emission cross sections for ^{209}Bi, at 60°, with incident neutron energy of 14.1 MeV.

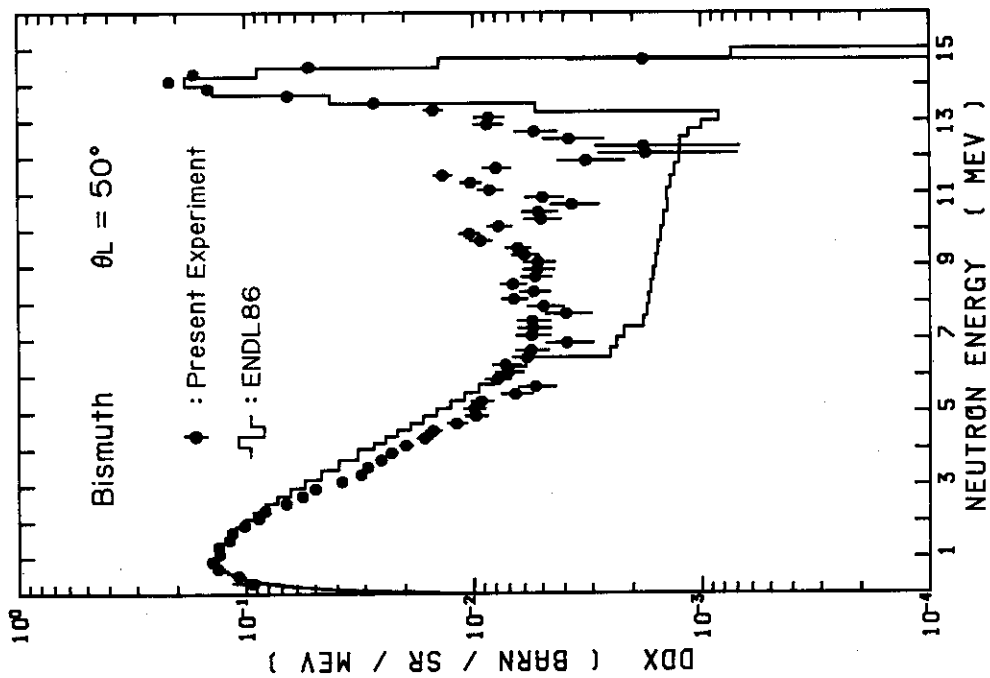

Fig.DF-5 Double differential neutron emission cross sections for ^{209}Bi, at 50°, with incident neutron energy of 14.1 MeV.

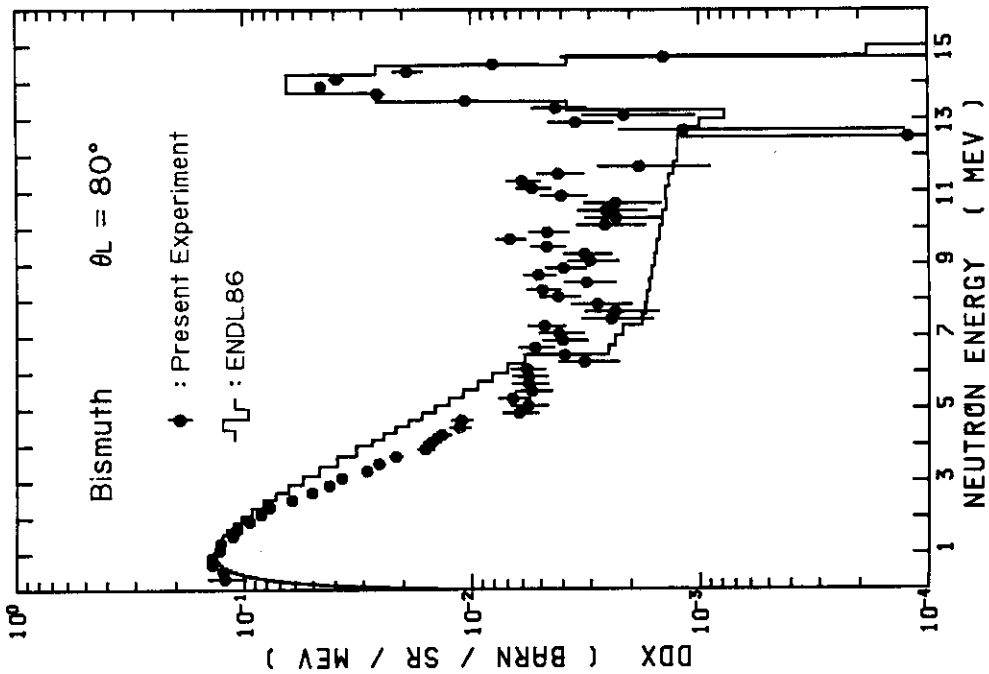

Fig.DF-8 Double differential neutron emission cross sections for ^{209}Bi, at 80°, with incident neutron energy of 14.1 MeV.

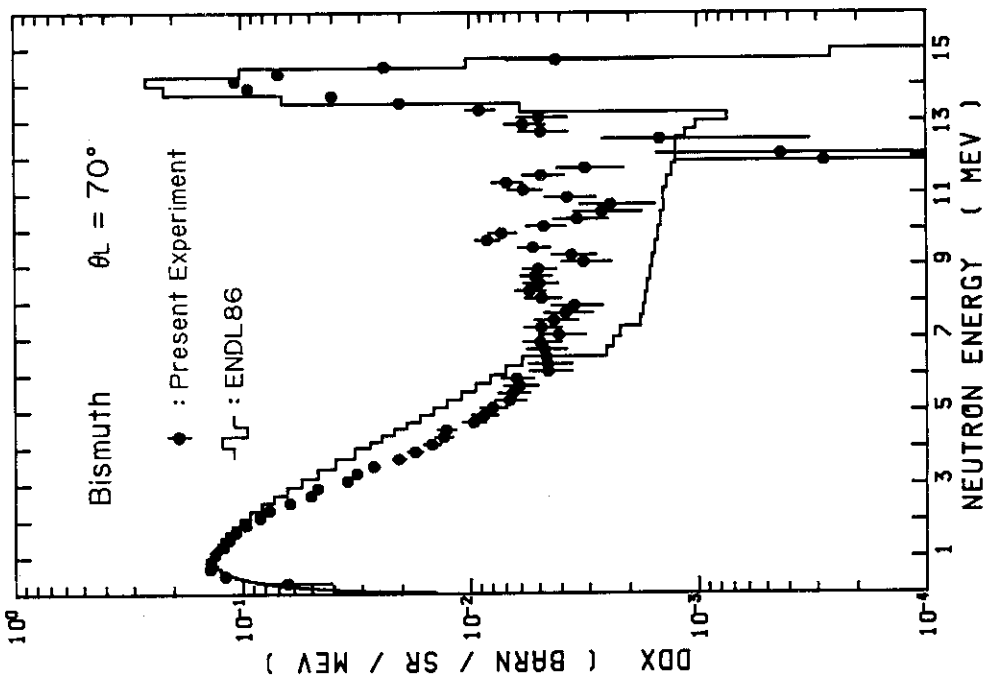

Fig.DF-7 Double differential neutron emission cross sections for ^{209}Bi, at 70°, with incident neutron energy of 14.1 MeV.

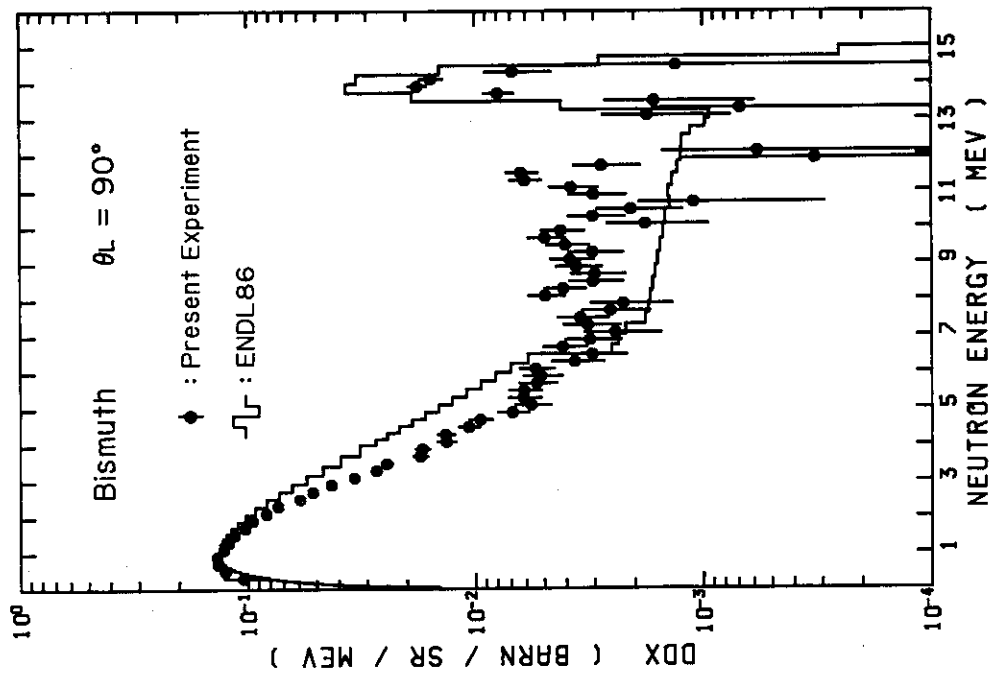

Fig.DF-9 Double differential neutron emission cross sections for ^{209}Bi, at 90°, with incident neutron energy of 14.1 MeV.

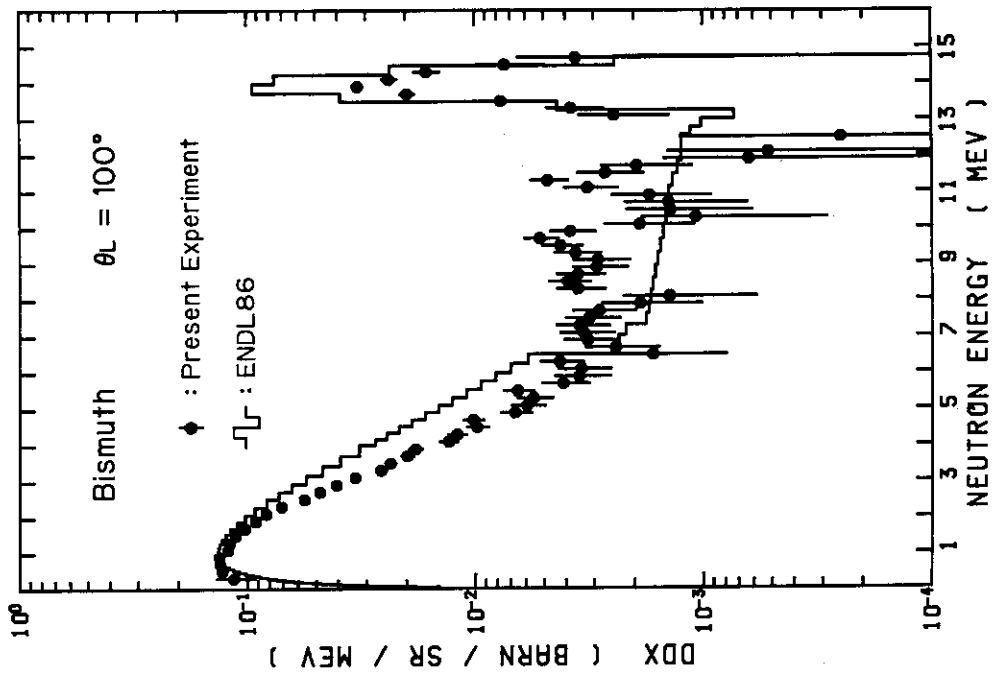

Fig.DF-10 Double differential neutron emission cross sections for ^{209}Bi, at 100°, with incident neutron energy of 14.1 MeV.

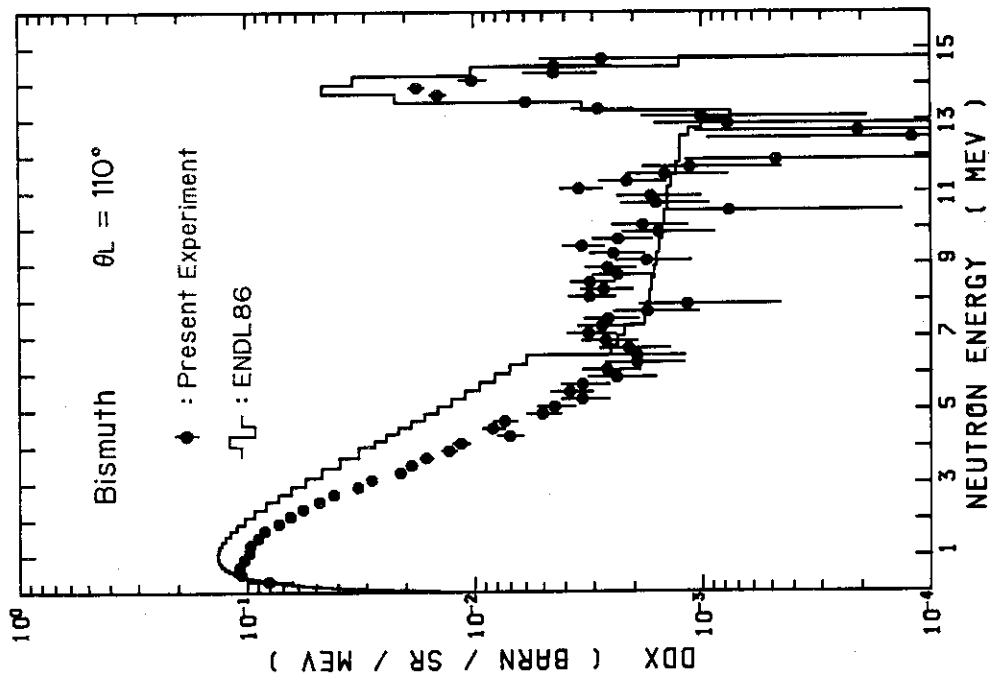

Fig.DF-11 Double differential neutron emission cross sections for ^{209}Bi, at 110°, with incident neutron energy of 14.1 MeV.

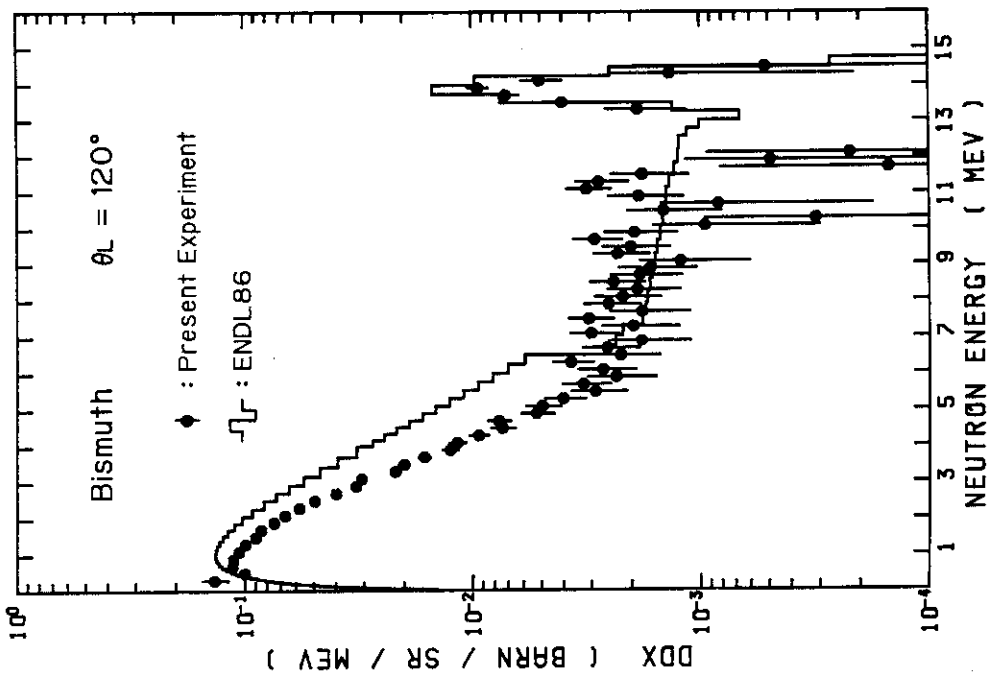

Fig.DF-12 Double differential neutron emission cross sections for ^{209}Bi, at 120°, with incident neutron energy of 14.1 MeV.

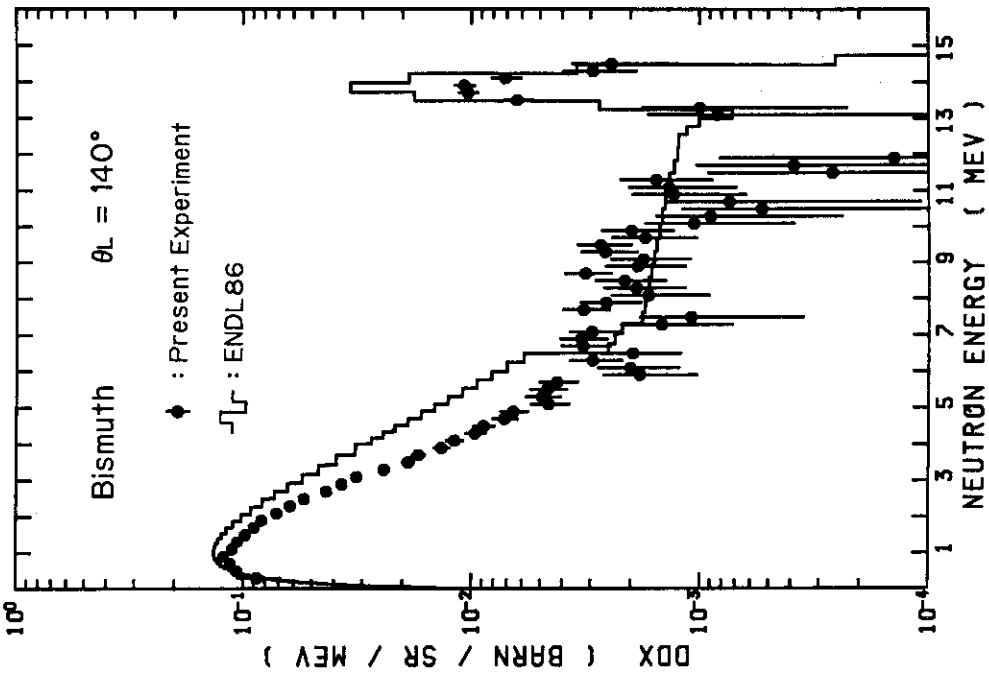

Fig.DF-14 Double differential neutron emission cross sections for ^{209}Bi, at 140°, with incident neutron energy of 14.1 MeV.

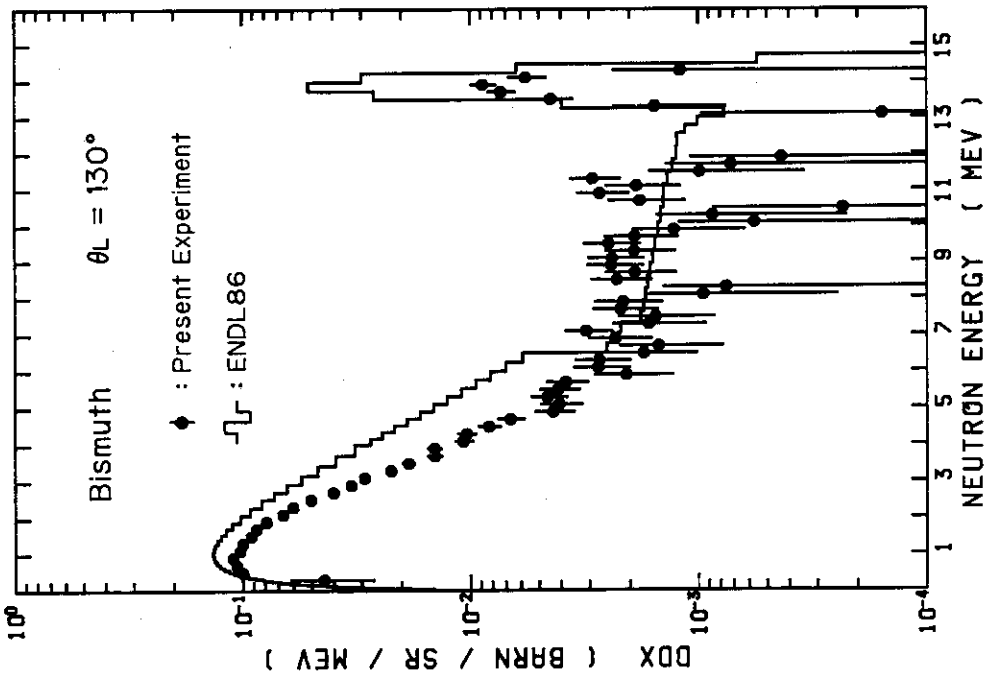

Fig.DF-13 Double differential neutron emission cross sections for ^{209}Bi, at 130°, with incident neutron energy of 14.1 MeV.

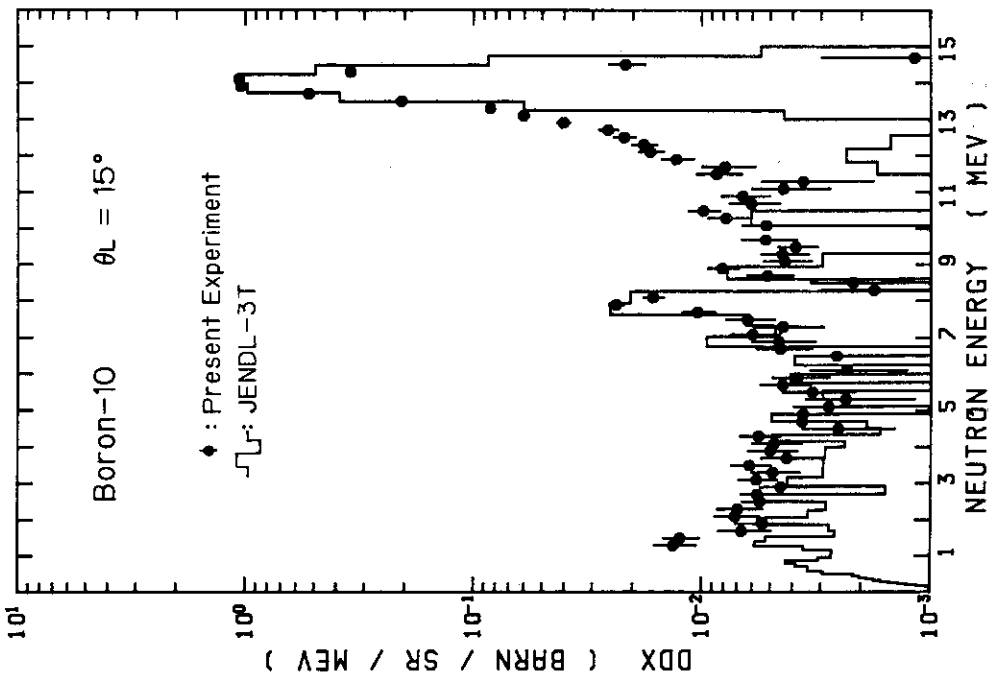

Fig.DF-16 Double differential neutron emission cross sections for ^{10}B, at 15°, with incident neutron energy of 14.1 MeV.

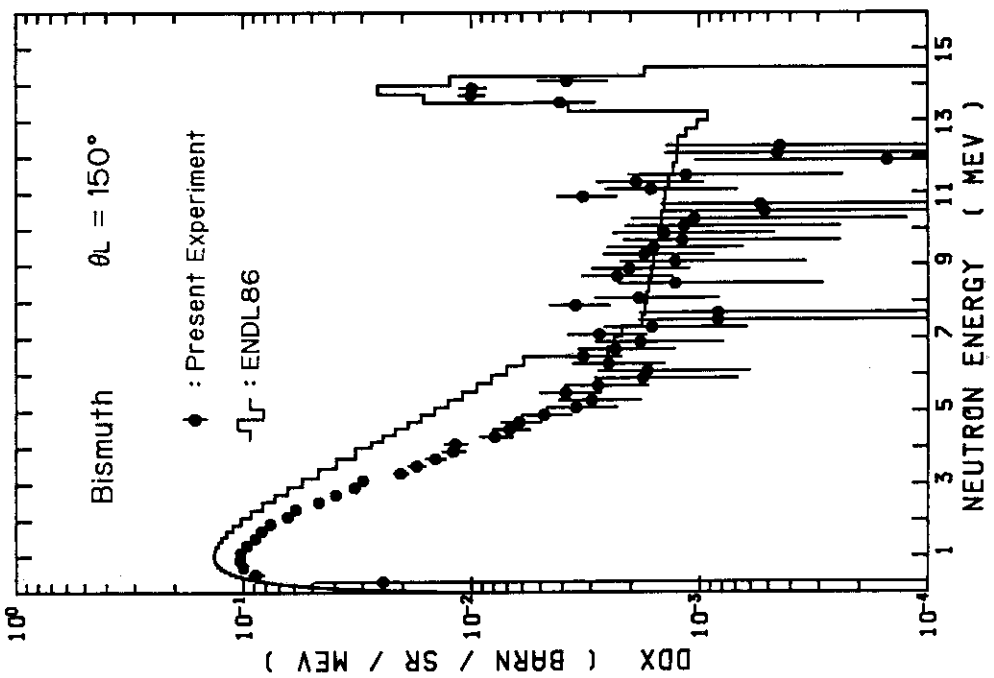

Fig.DF-15 Double differential neutron emission cross sections for ^{209}Bi, at 150°, with incident neutron energy of 14.1 MeV.

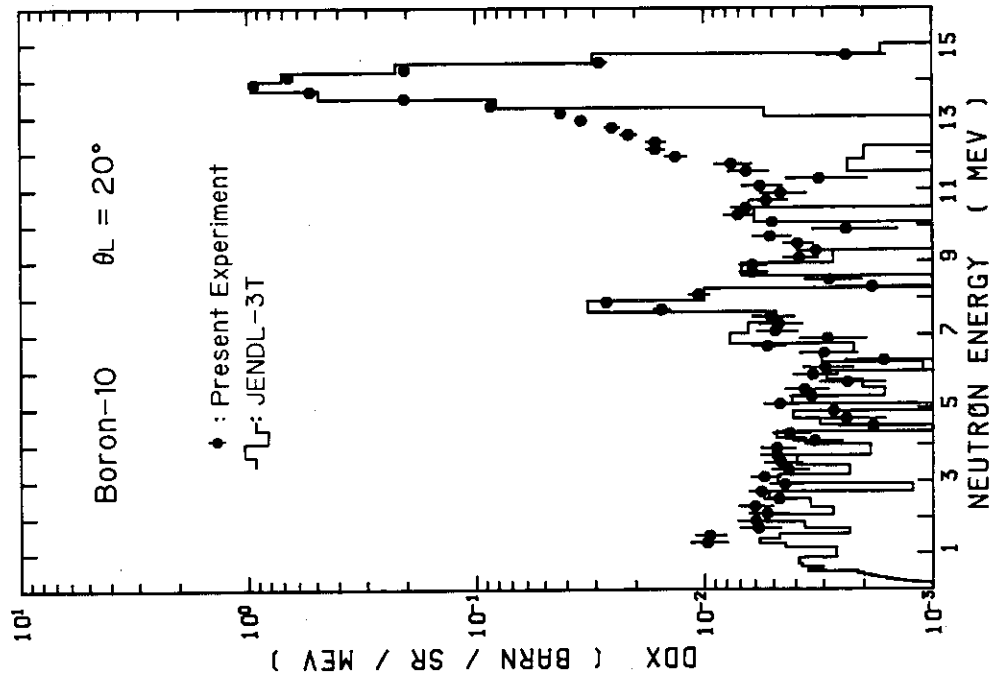

Fig.DF-17 Double differential neutron emission cross sections for ^{10}B, at 20°, with incident neutron energy of 14.1 MeV.

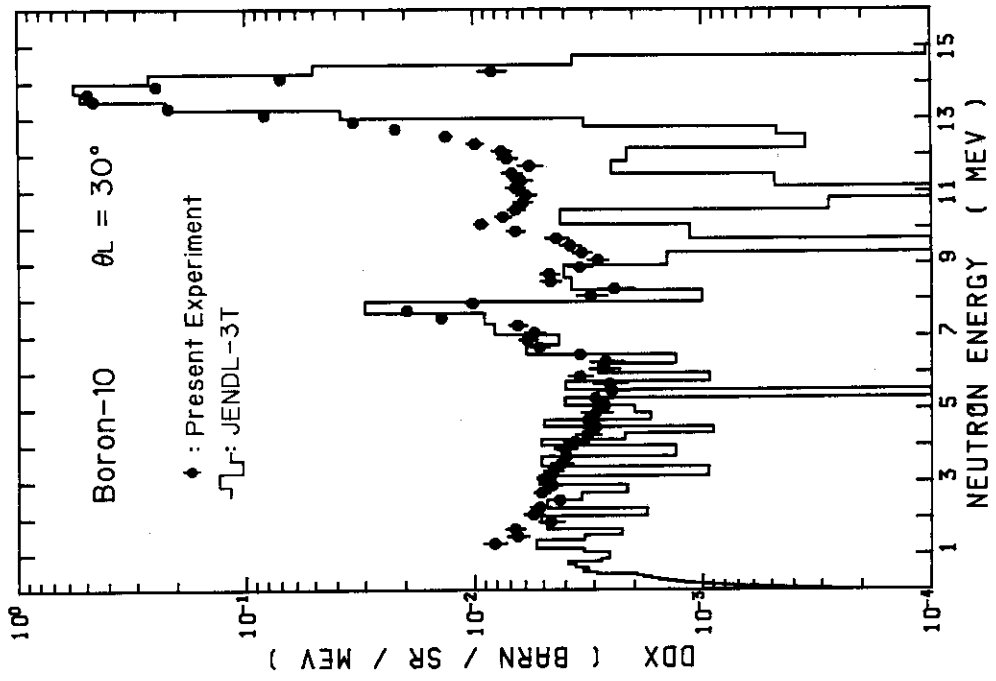

Fig.DF-18 Double differential neutron emission cross sections for ^{10}B, at 30°, with incident neutron energy of 14.1 MeV.

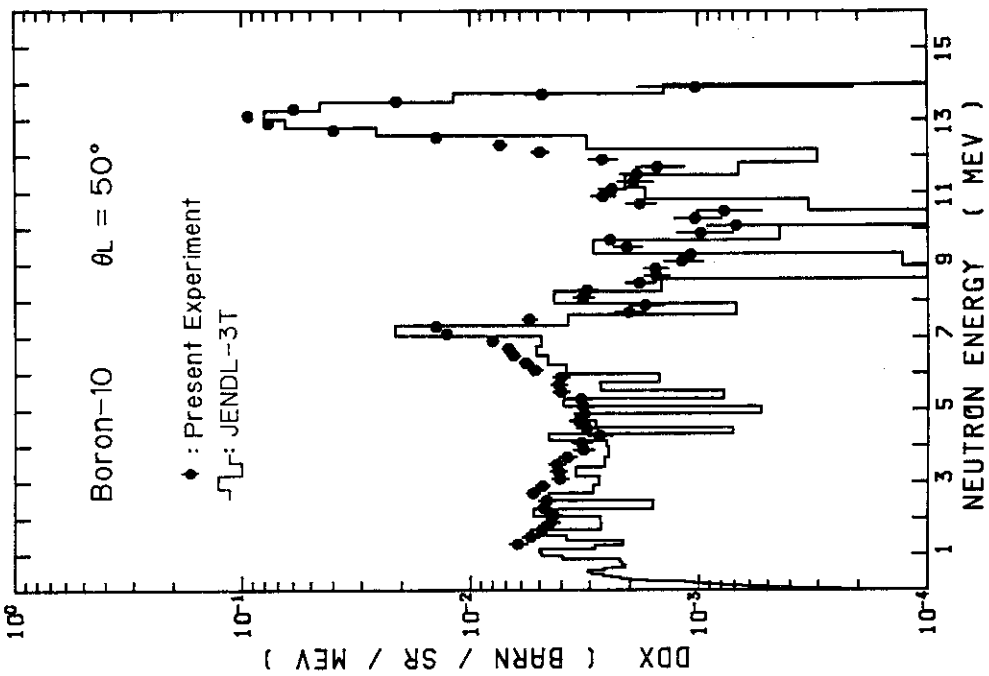

Fig.DF-20 Double differential neutron emission cross sections for ^{10}B, at 50°, with incident neutron energy of 14.1 MeV.

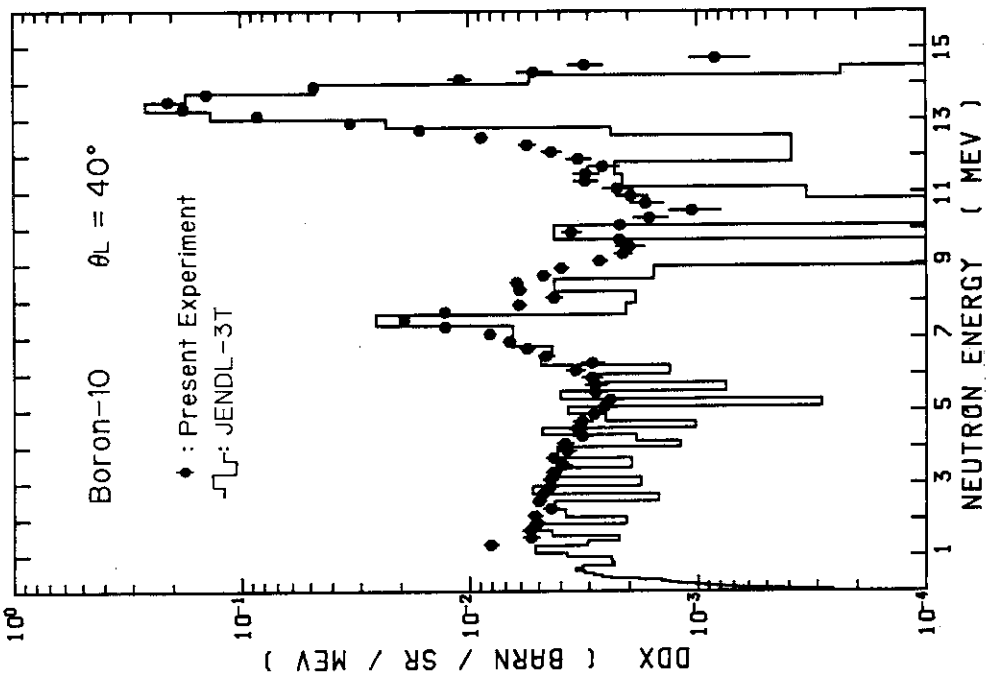

Fig.DF-19 Double differential neutron emission cross sections for ^{10}B, at 40°, with incident neutron energy of 14.1 MeV.

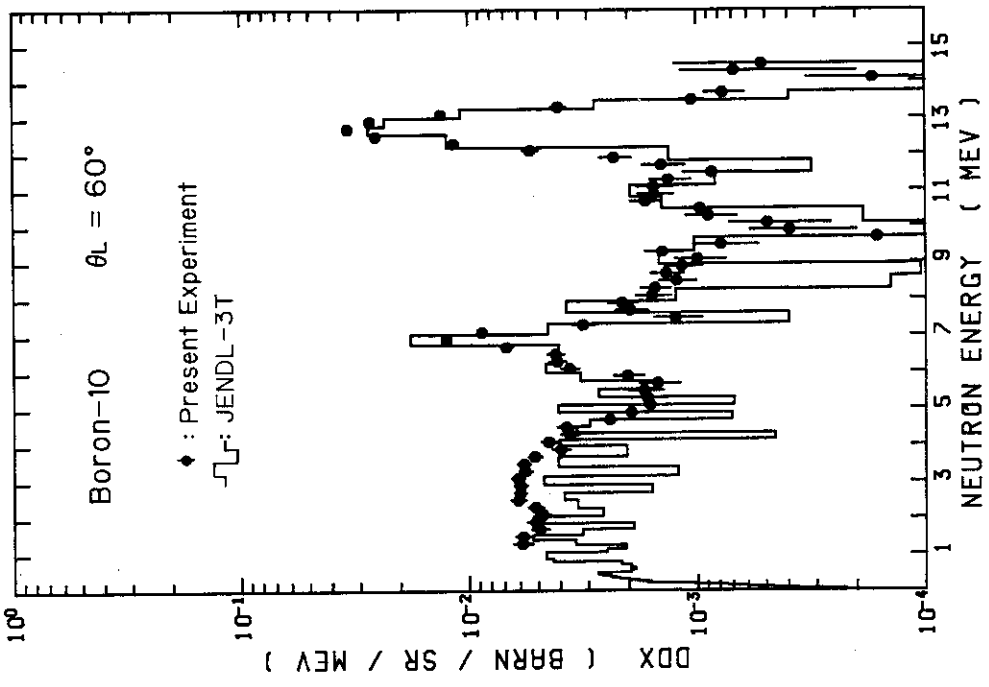

Fig.DF-21 Double differential neutron emission cross sections for ^{10}B, at 60°, with incident neutron energy of 14.1 MeV.

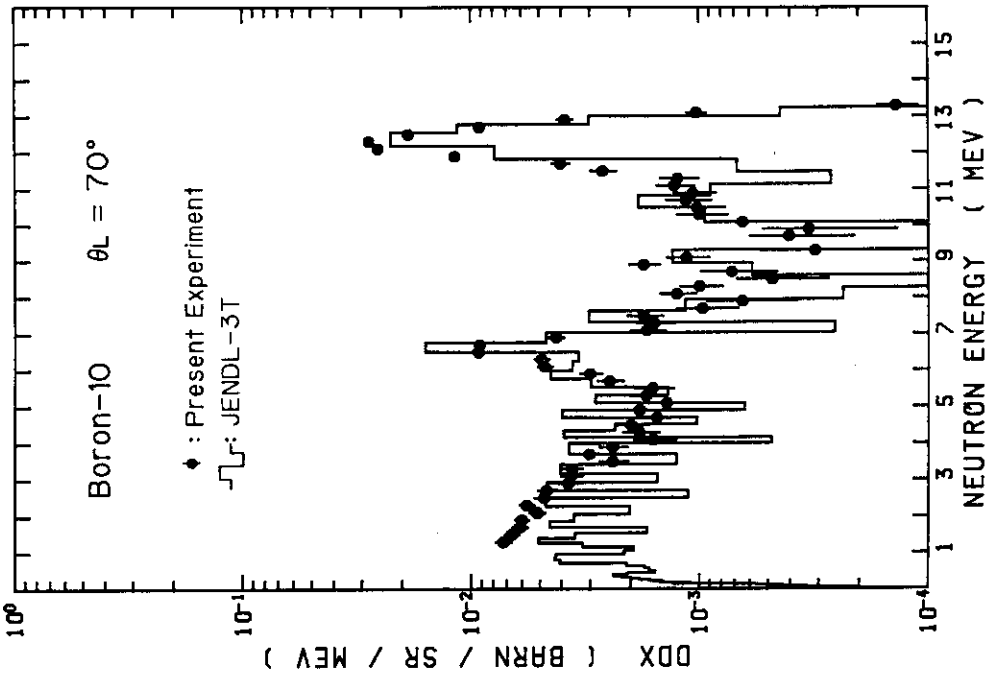

Fig.DF-22 Double differential neutron emission cross sections for ^{10}B, at 70°, with incident neutron energy of 14.1 MeV.

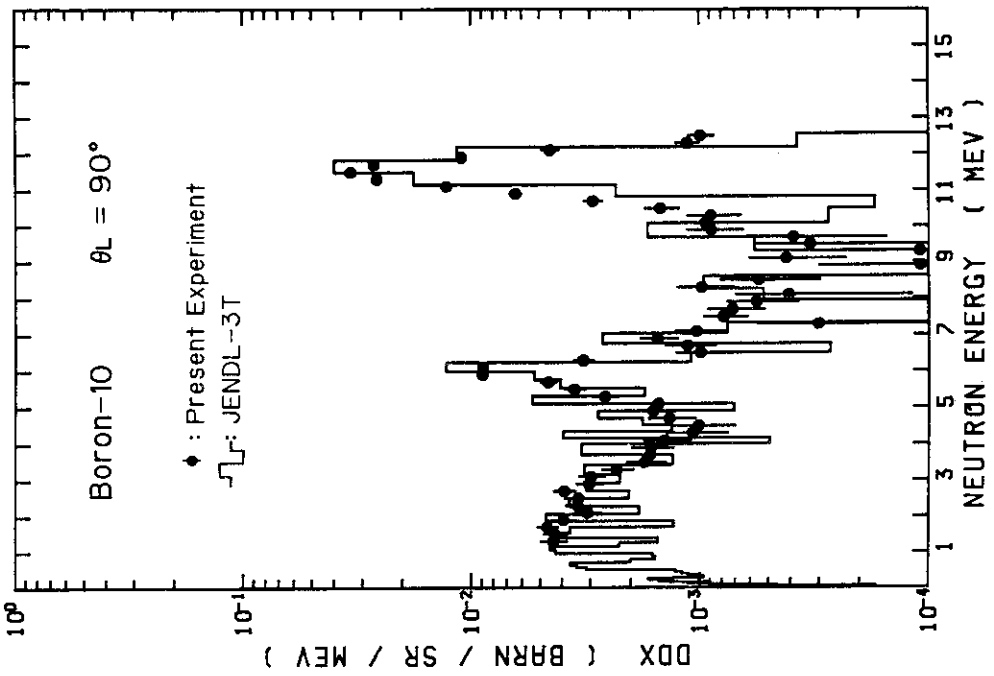

Fig.DF-24 Double differential neutron emission cross sections for ^{10}B, at 90°, with incident neutron energy of 14.1 MeV.

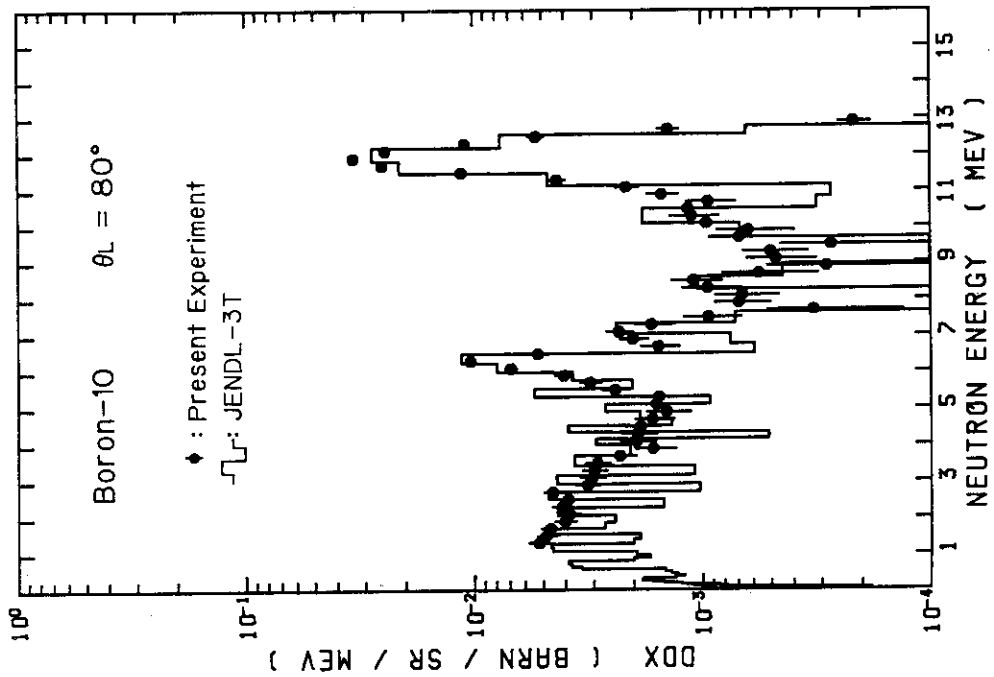

Fig.DF-23 Double differential neutron emission cross sections for ^{10}B, at 80°, with incident neutron energy of 14.1 MeV.

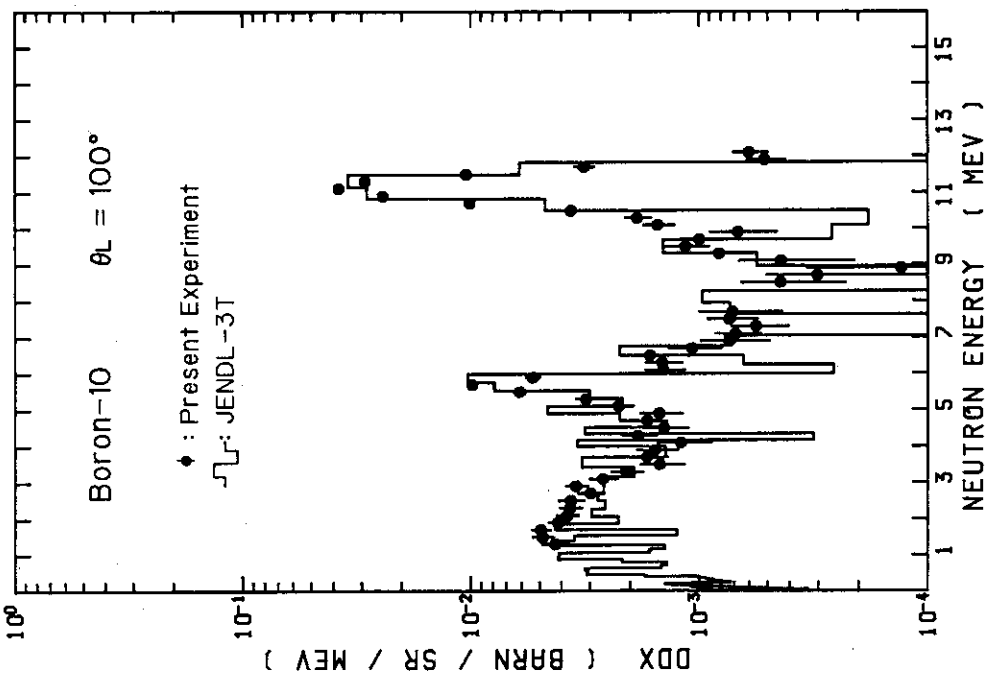

Fig.DF-25 Double differential neutron emission cross sections for ^{10}B, at 100°, with incident neutron energy of 14.1 MeV.

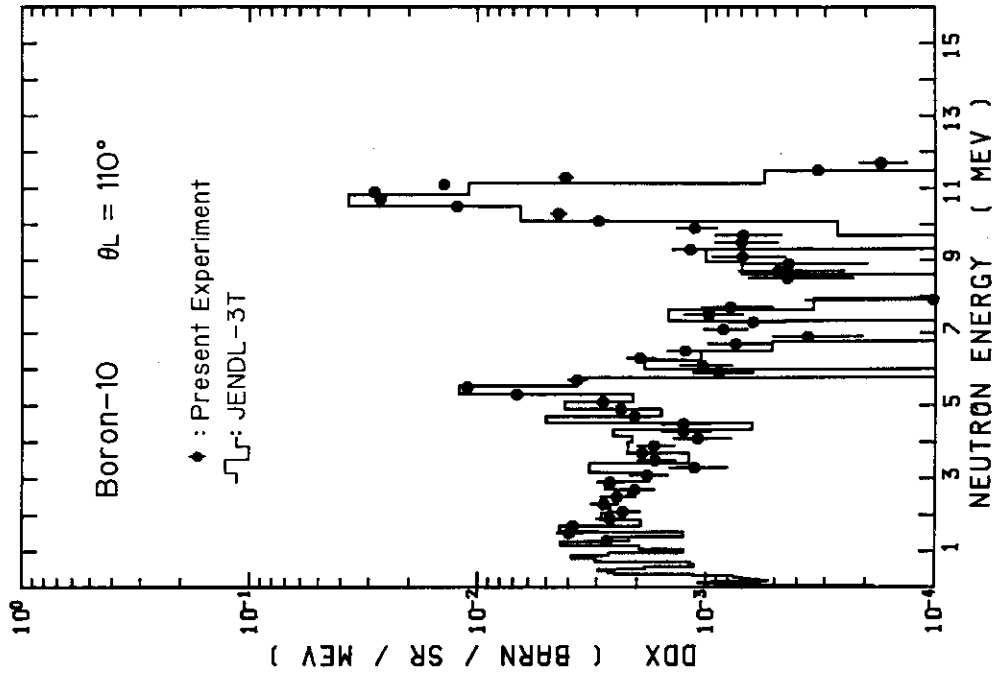

Fig.DF-26 Double differential neutron emission cross sections for ^{10}B, at 110°, with incident neutron energy of 14.1 MeV.

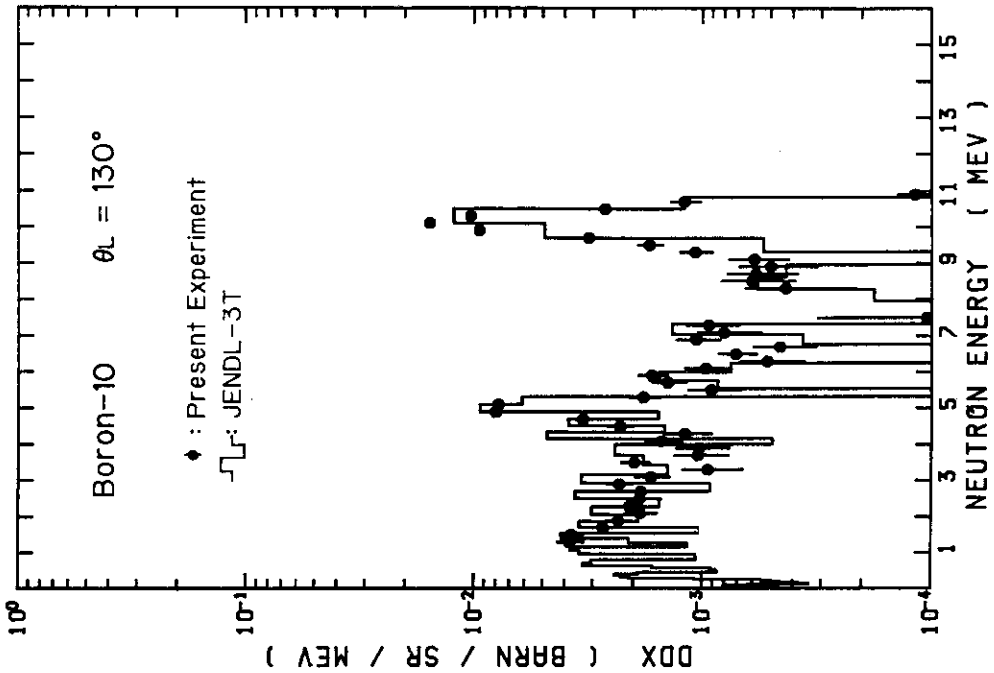

Fig.DF-28 Double differential neutron emission cross sections for ^{10}B, at 130°, with incident neutron energy of 14.1 MeV.

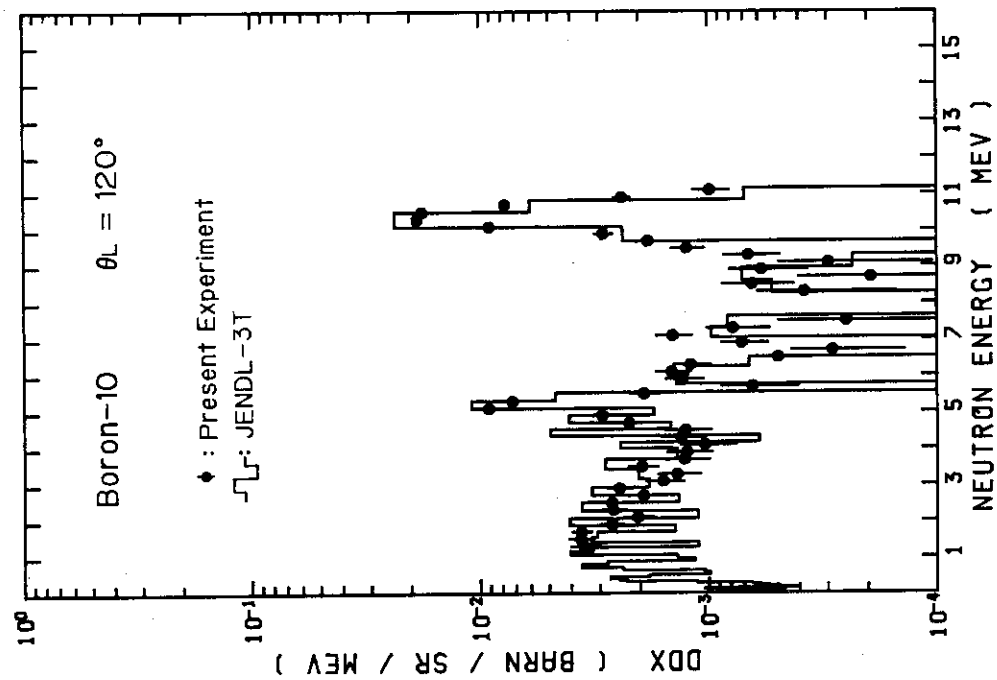

Fig.DF-27 Double differential neutron emission cross sections for ^{10}B, at 120°, with incident neutron energy of 14.1 MeV.

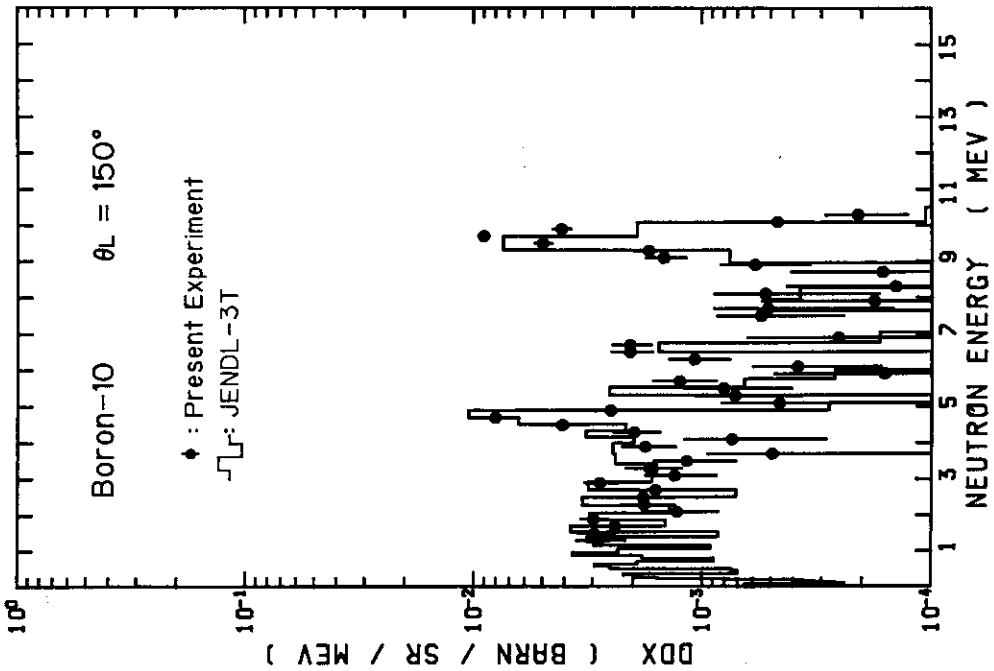

Fig.DF-30 Double differential neutron emission cross sections for ^{10}B, at 150°, with incident neutron energy of 14.1 MeV.

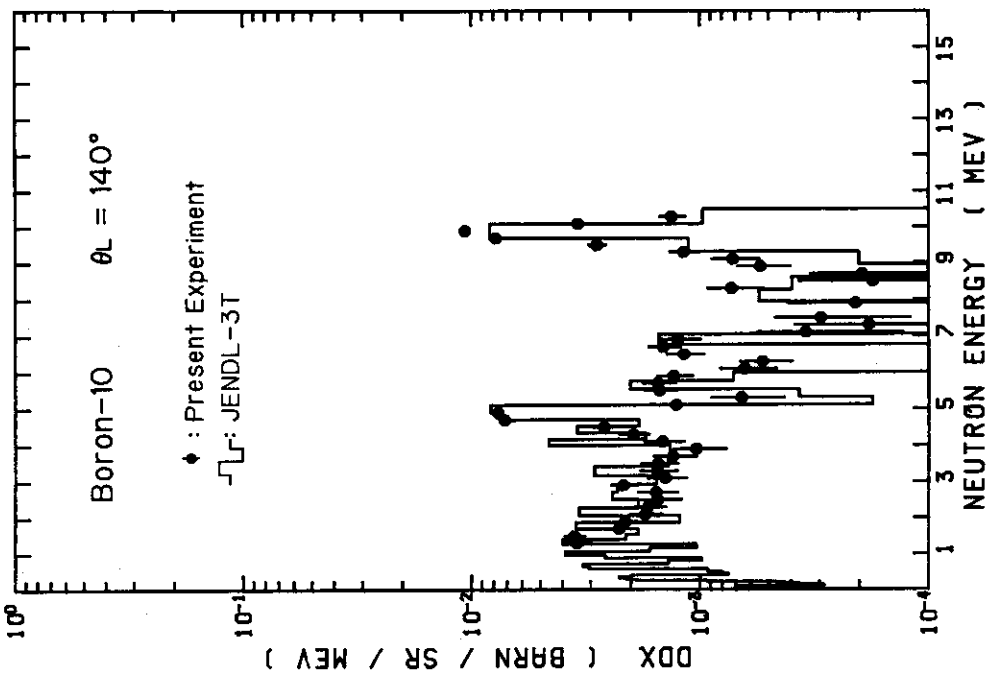

Fig.DF-29 Double differential neutron emission cross sections for ^{10}B, at 140°, with incident neutron energy of 14.1 MeV.

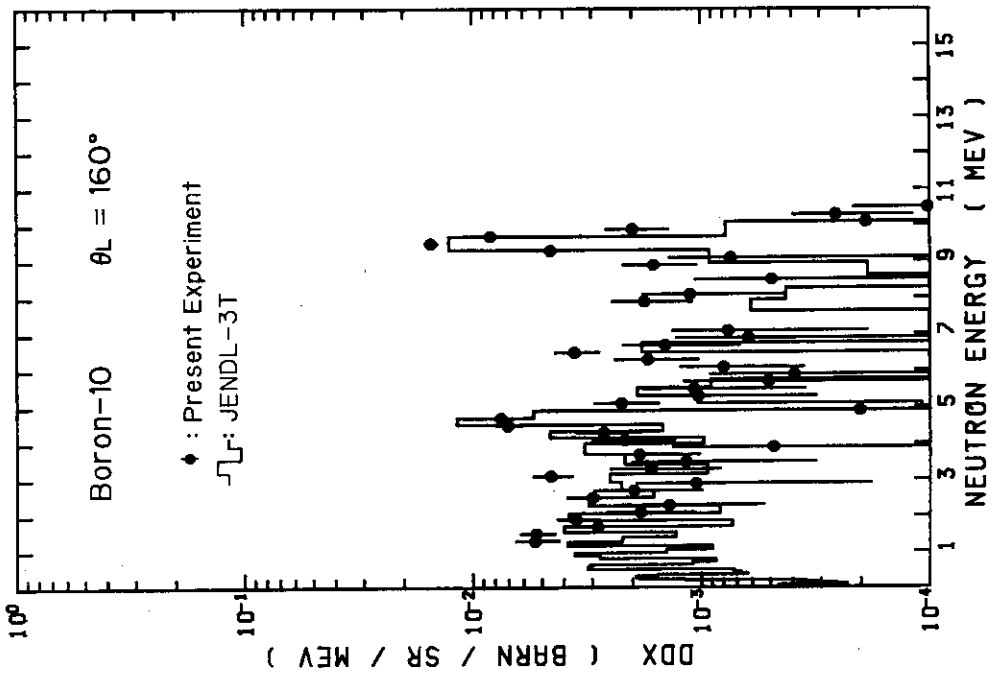

Fig.DF-31 Double differential neutron emission cross sections for ^{10}B, at 160°, with incident neutron energy of 14.1 MeV.

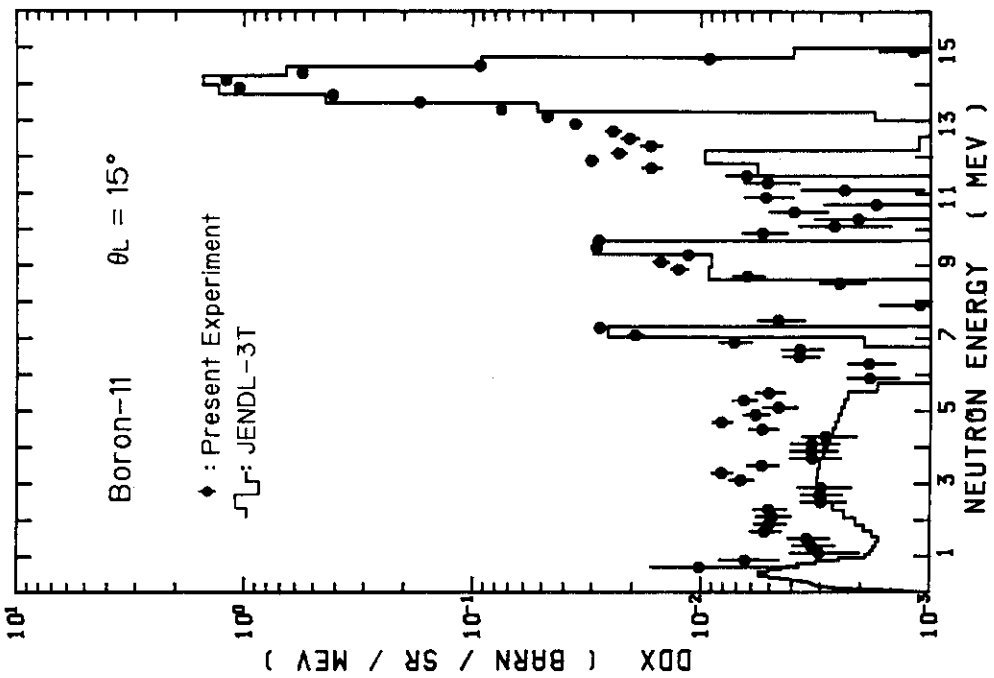

Fig.DF-32 Double differential neutron emission cross sections for ^{11}B, at 15°, with incident neutron energy of 14.1 MeV.

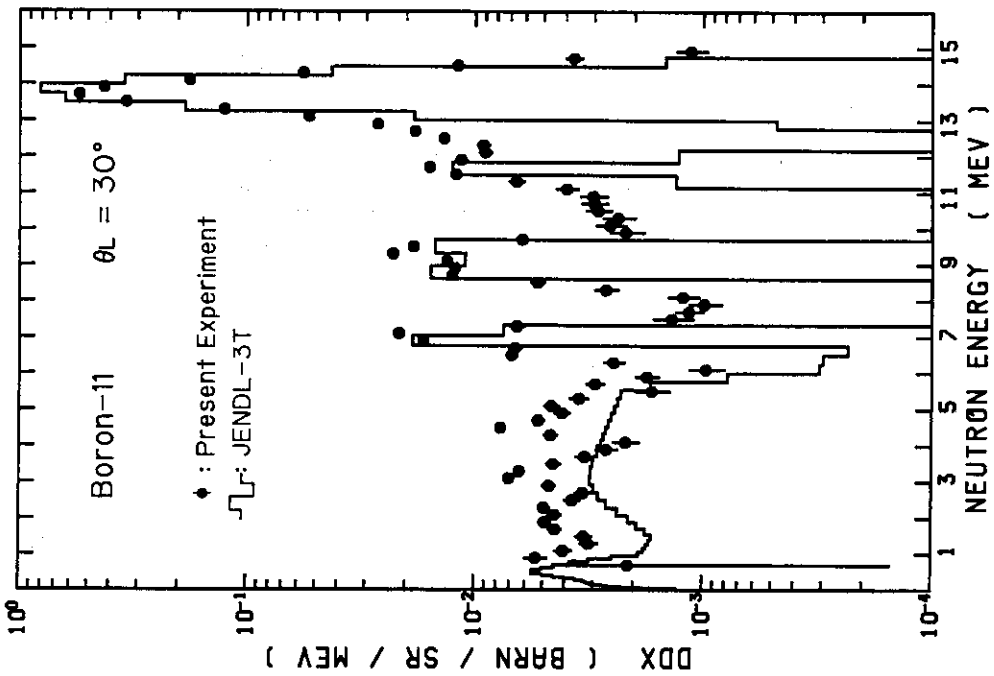

Fig.DF-34 Double differential neutron emission cross sections for ^{11}B, at 30°, with incident neutron energy of 14.1 MeV.

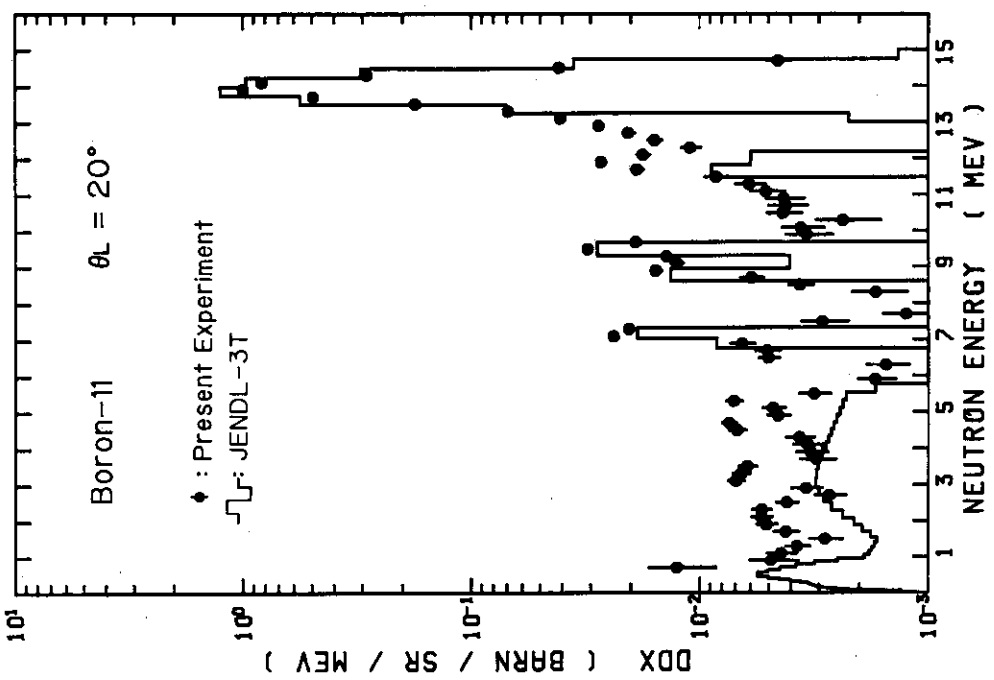

Fig.DF-33 Double differential neutron emission cross sections for ^{11}B, at 20°, with incident neutron energy of 14.1 MeV.

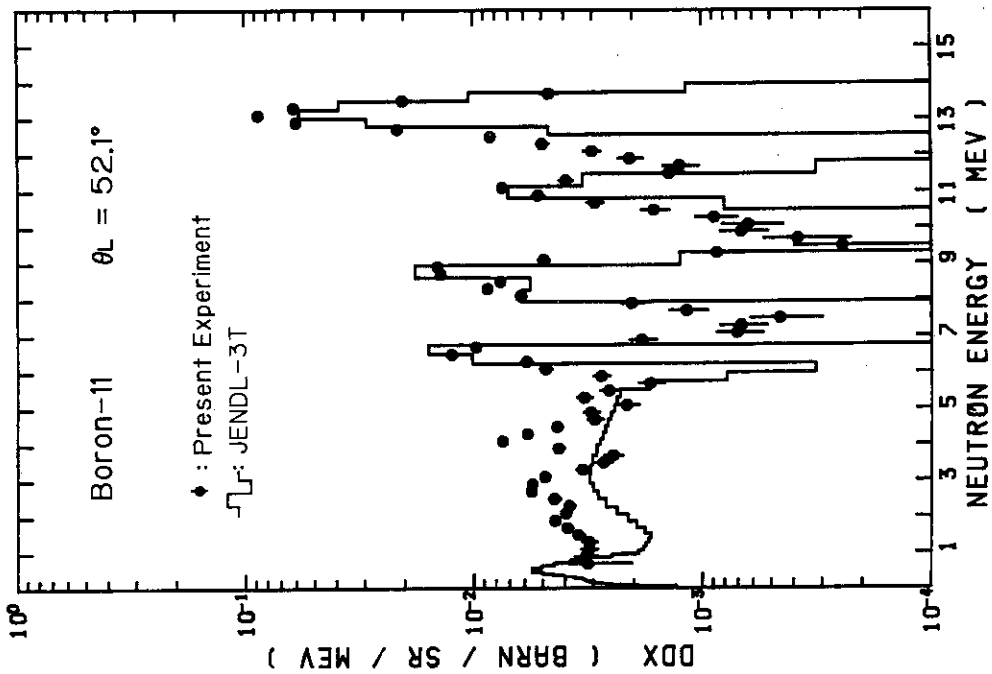

Fig.DF-36 Double differential neutron emission cross sections for ^{11}B, at 52.1°, with incident neutron energy of 14.1 MeV.

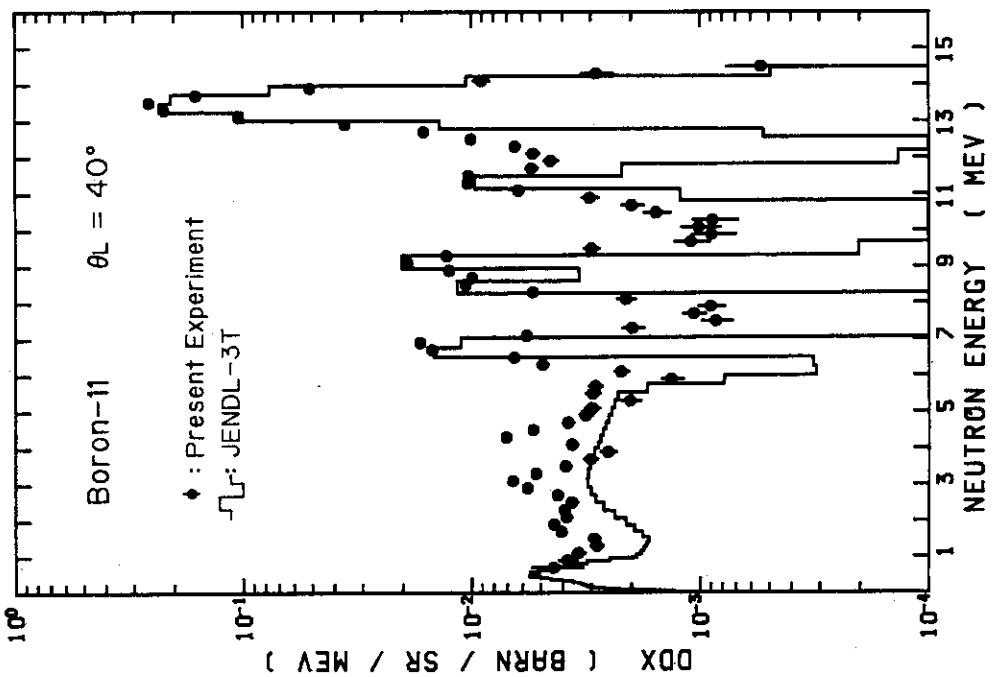

Fig.DF-35 Double differential neutron emission cross sections for ^{11}B, at 40°, with incident neutron energy of 14.1 MeV.

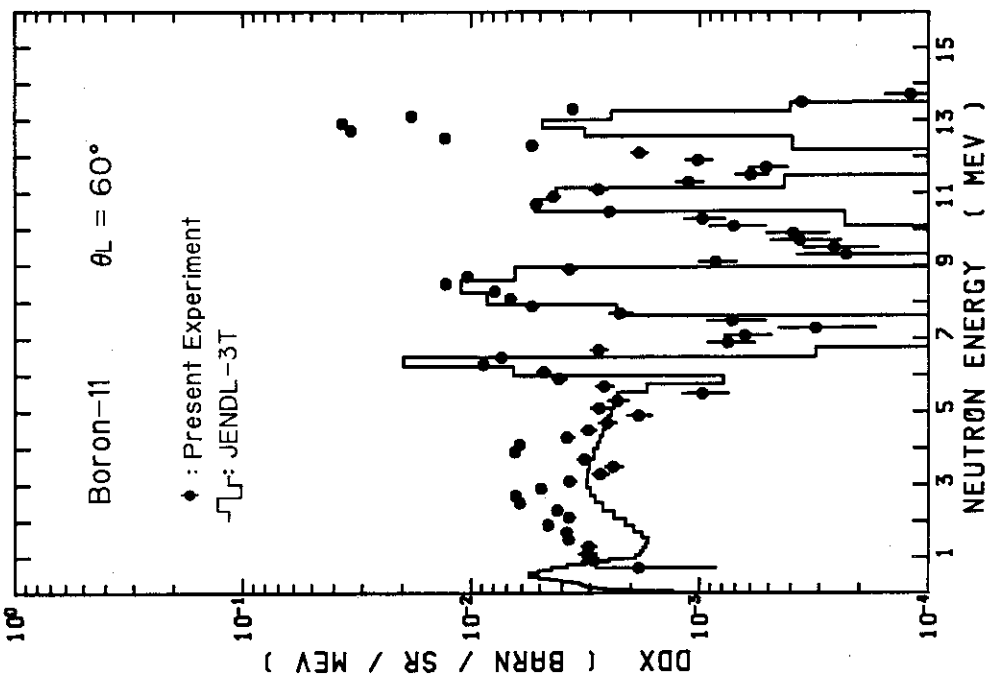

Fig.DF-37 Double differential neutron emission cross sections for ^{11}B, at 60°, with incident neutron energy of 14.1 MeV.

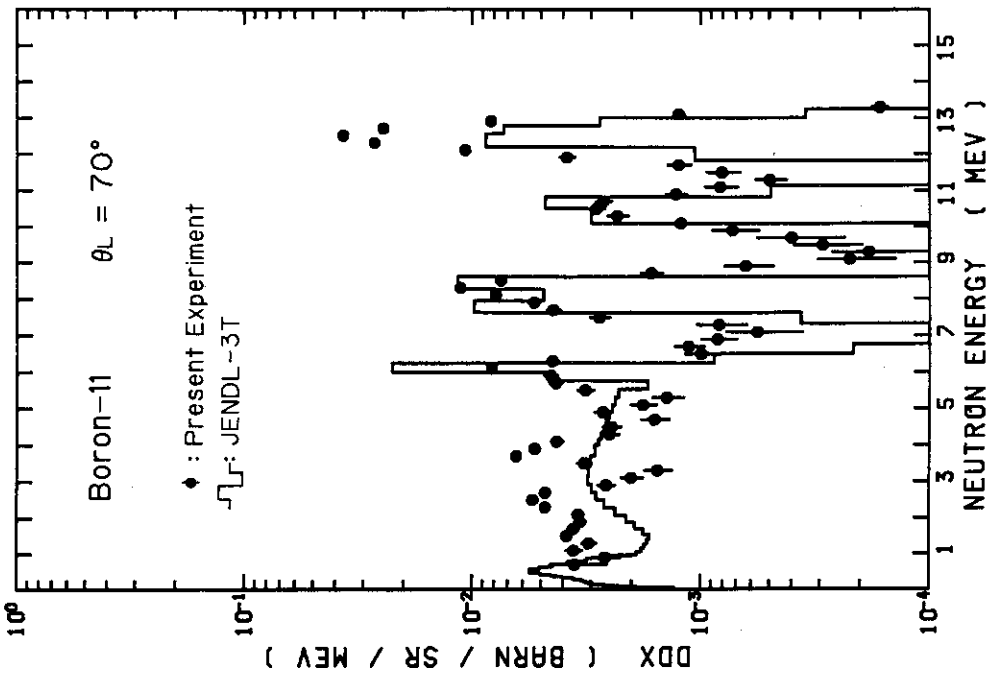

Fig.DF-38 Double differential neutron emission cross sections for ^{11}B, at 70°, with incident neutron energy of 14.1 MeV.

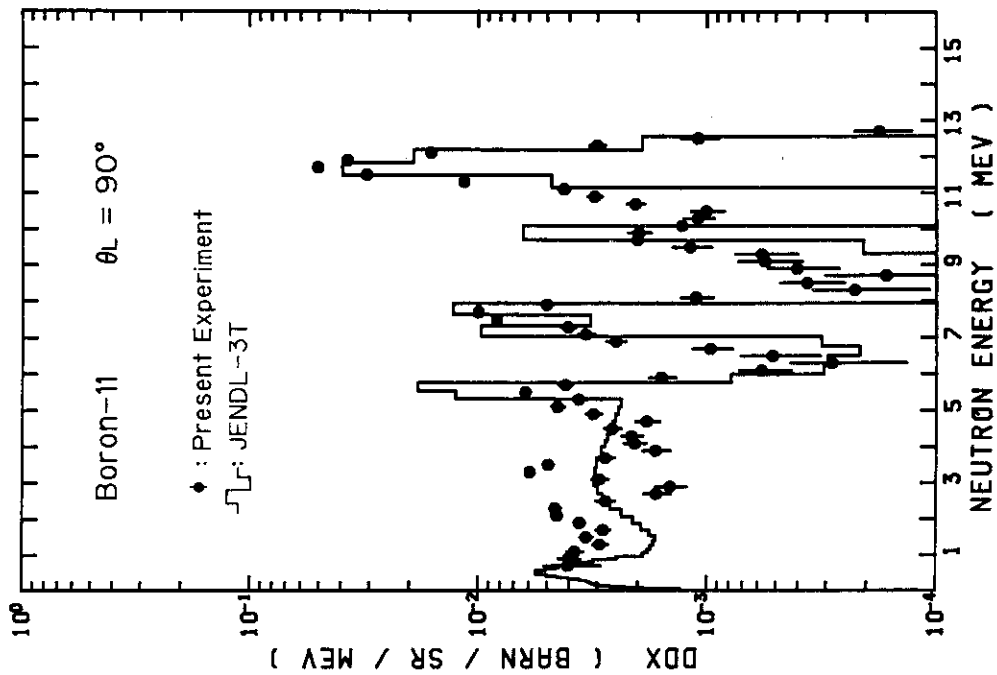

Fig.DF-40 Double differential neutron emission cross sections for ^{11}B, at 90°, with incident neutron energy of 14.1 MeV.

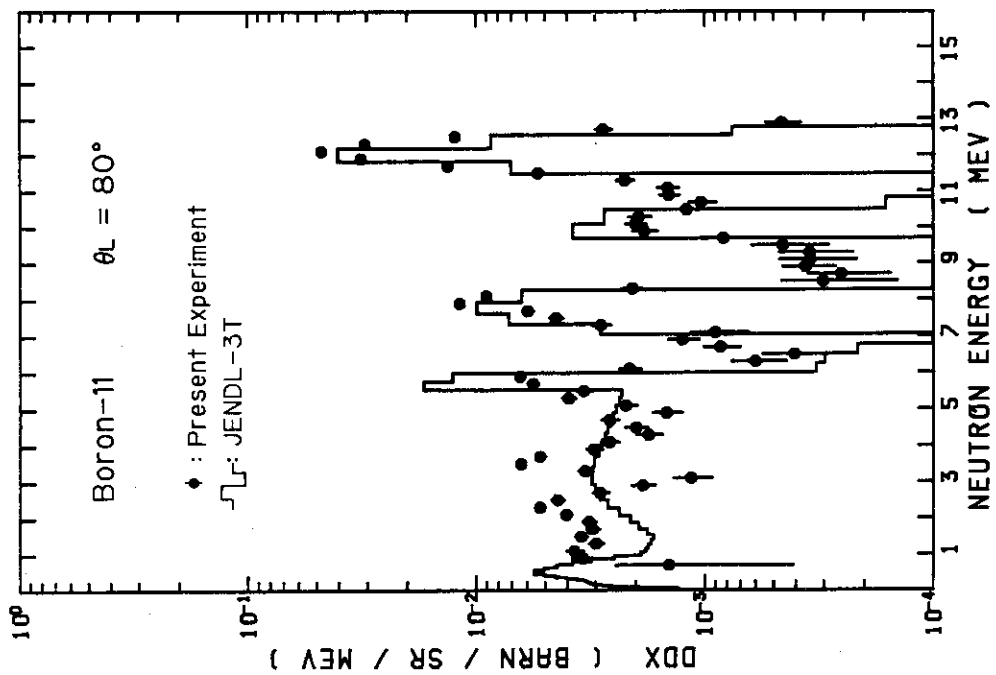

Fig.DF-39 Double differential neutron emission cross sections for ^{11}B, at 80°, with incident neutron energy of 14.1 MeV.

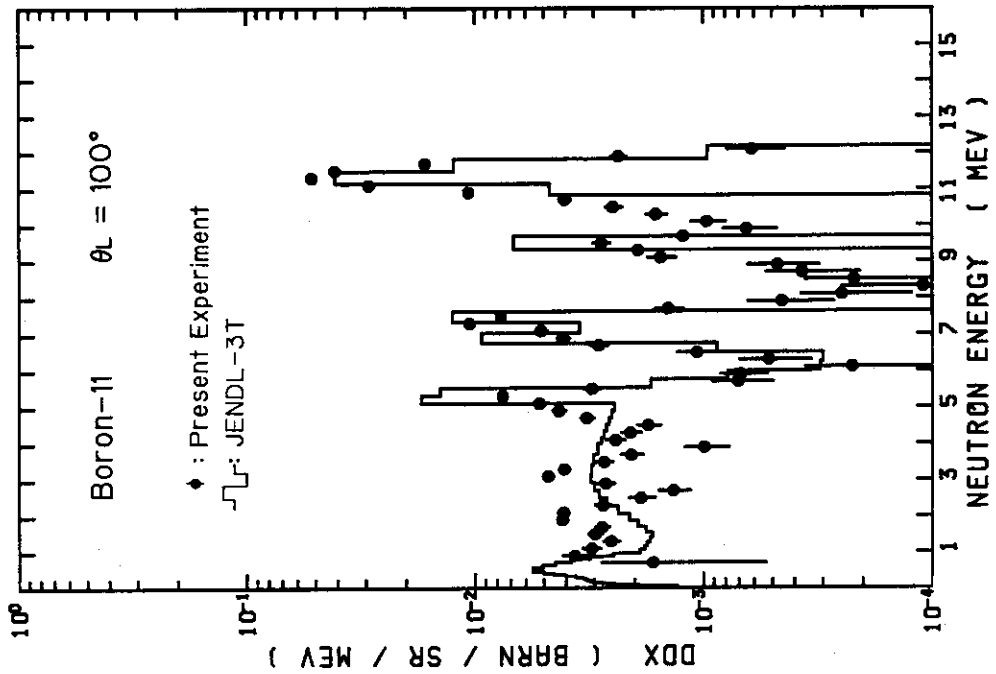

Fig.DF-41 Double differential neutron emission cross sections for ^{11}B, at 100°, with incident neutron energy of 14.1 MeV.

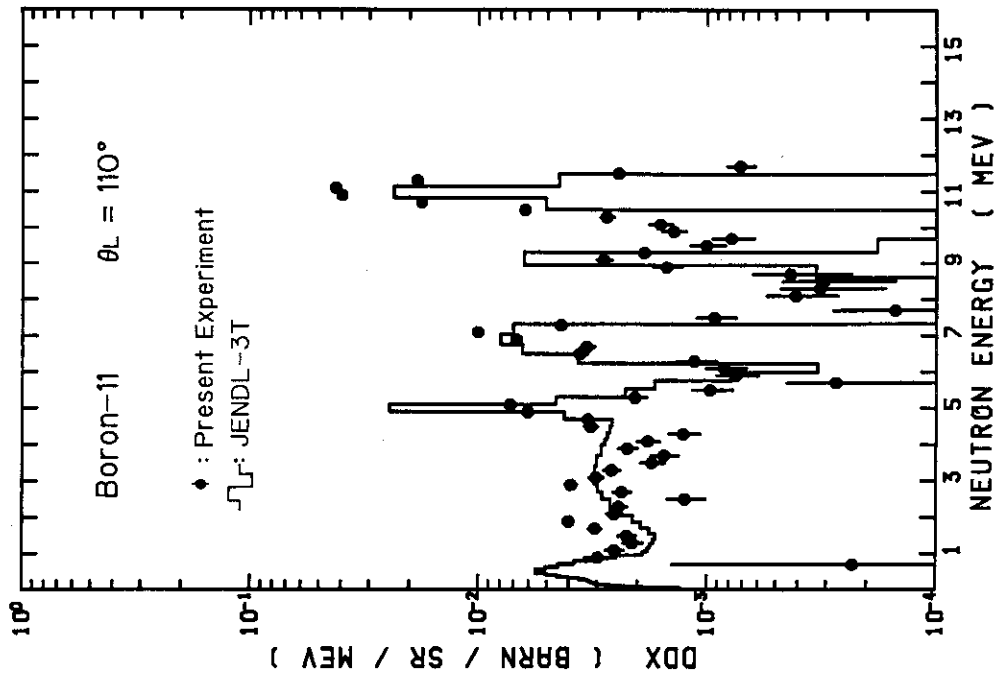

Fig.DF-42 Double differential neutron emission cross sections for ^{11}B, at 110°, with incident neutron energy of 14.1 MeV.

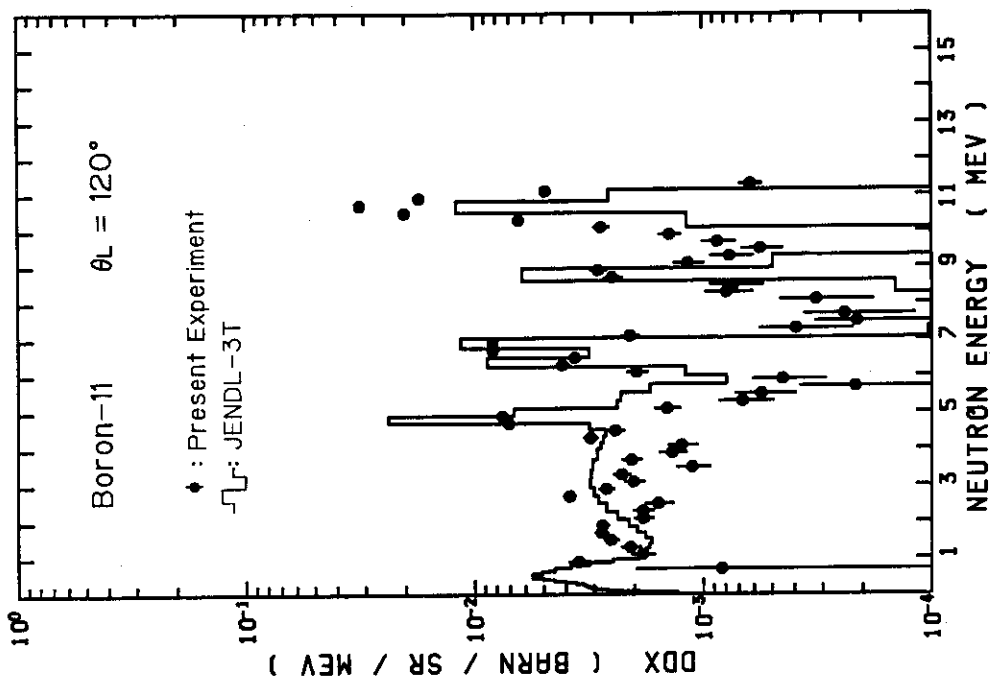

Fig.DF-43 Double differential neutron emission cross sections for ^{11}B, at 120°, with incident neutron energy of 14.1 MeV.

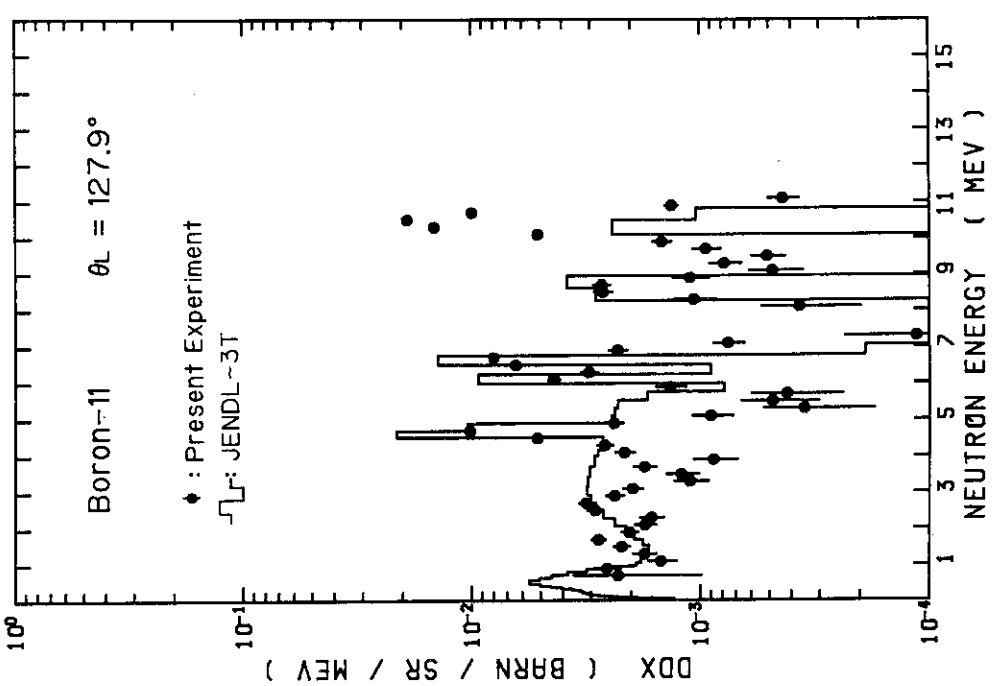

Fig.DF-44 Double differential neutron emission cross sections for ^{11}B, at 127.9°, with incident neutron energy of 14.1 MeV.

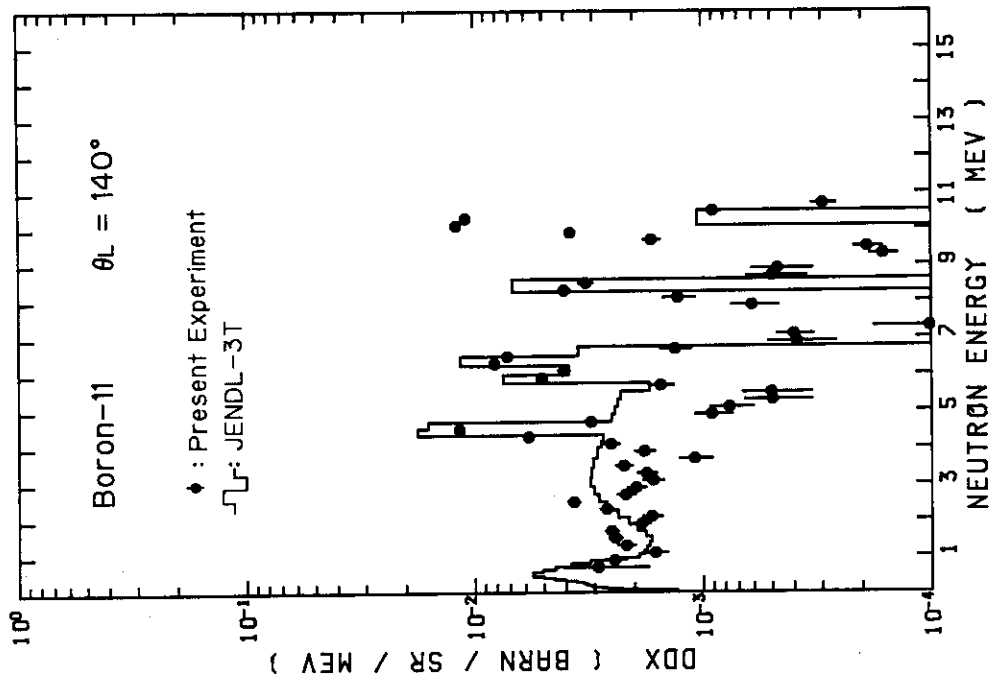

Fig.DF-45 Double differential neutron emission cross sections for ^{11}B, at 140°, with incident neutron energy of 14.1 MeV.

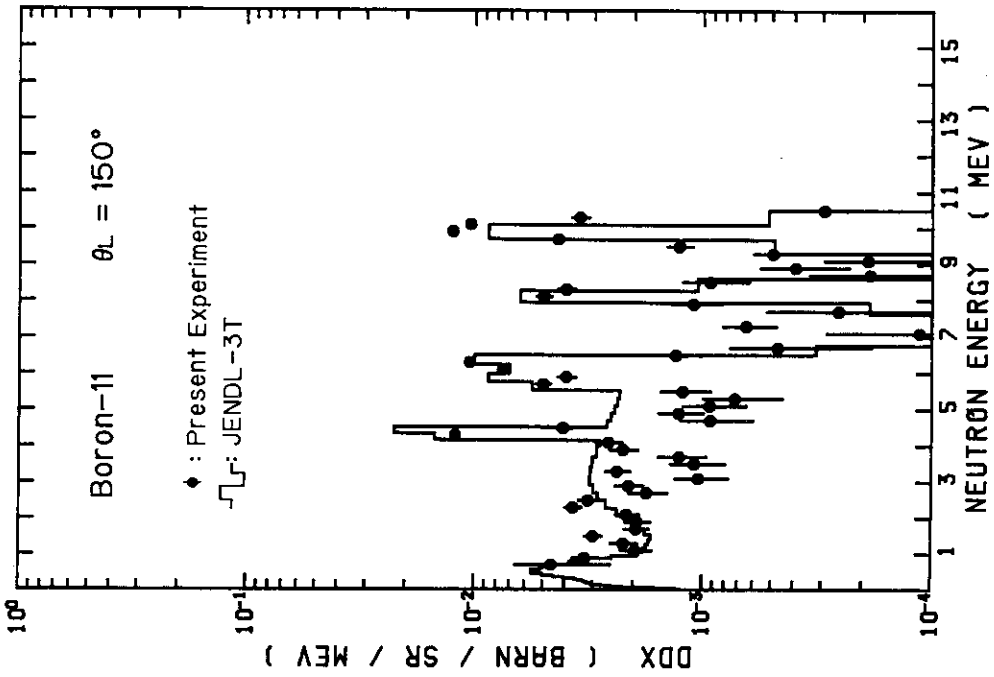

Fig.DF-46 Double differential neutron emission cross sections for ^{11}B, at 150°, with incident neutron energy of 14.1 MeV.

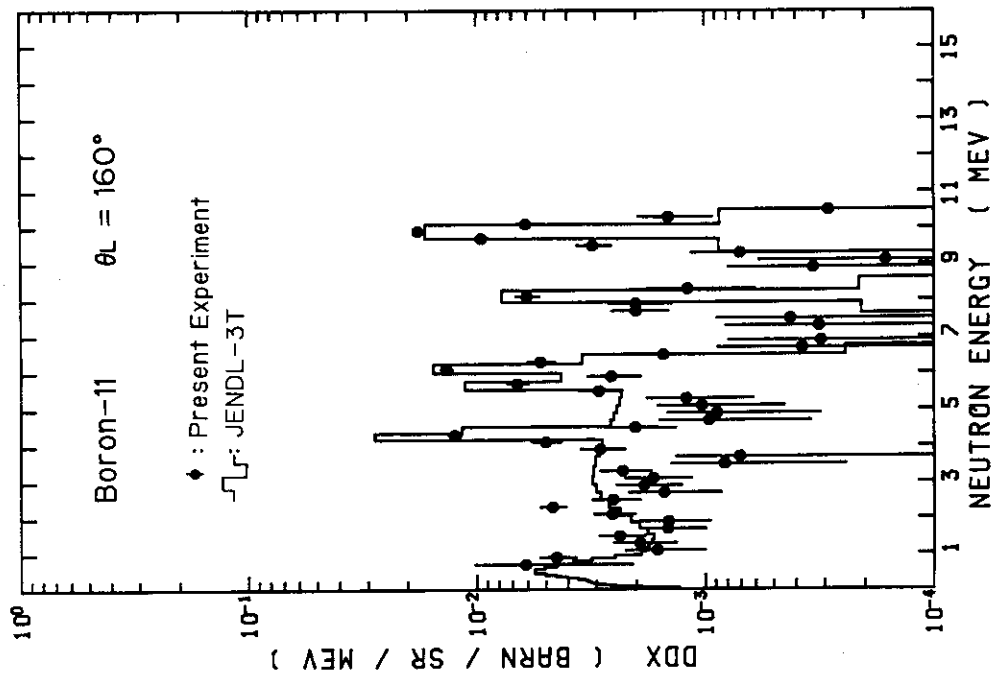

Fig.DF-47 Double differential neutron emission cross sections for ^{11}B, at 160°, with incident neutron energy of 14.1 MeV.